ANTHROPOGENIC SIGNALS OBSERVED USING INTERFEROMETRIC SYNTHETIC APERTURE RADAR IN THE PACIFIC NORTHWEST

A Thesis

Presented to the Faculty of the Graduate School

of Cornell University

In Partial Fulfillment of the Requirements for the Degree of

Master of Science

by

Veronica Blythe Prush

August 2013

ABSTRACT

Interferometric Synthetic Aperture Radar (InSAR) has developed over the past few decades as a tool with many applications to studies of crustal deformation. This thesis focuses on two signals observed in interferograms covering the Pacific Northwest. A prominent signal observed in many interferograms covering the region is associated with the logging of forests. We make use of the dependence of the topographic component of interferometric phase on the spatial separation between the sensor's locations at the two times of image acquisition to determine the height of scattering elements within vegetated regions, taken to be a proxy for canopy height. A second signal is associated with the transport of material due to the operations of the Centralia power plant and mine in Centralia, Washington. We estimate the volume and time history of material displacement for the area surrounding the power plant.

BIOGRAPHICAL SKETCH

Veronica Prush graduated from Stuyvesant High School in New York City in 2006 and enrolled at Juniata College in Huntingdon, Pennsylvania the following fall. During her sophomore year at Juniata she studied abroad at the Universidad San Francisco de Quito in Ecuador. While participating in a field excursion for her Volcanology class, she had the opportunity to witness an eruption of the active stratovolcano Tungurahua and, inspired by this event, she decided to pursue geology as her major. While completing her degree, she participated in the Research Experiences for Undergraduates (REU) program with the Center for Environmental Kinetics Analysis (CEKA) at the Pennsylvania State University in the summer of 2009, studying the effects of weathering on copper isotope profiles in the Marcellus Shale and associated soils. She graduated cum laude from Juniata in May 2010 with a bachelor of science in geology and a minor in Spanish.

Veronica began work on her master's thesis at Cornell University in August 2010. Her three years at Cornell were full of many wonderful opportunities. Highlights included a field course to Germany to study the geologic evidence of volcanism and the Ries impact crater and the opportunity to be in charge of the department's seismometer for a year. In her last year at Cornell University, she received the Estwing Award for Most Outstanding Graduate Student.

I dedicate this master's thesis to my parents, who have supported me unwaveringly.

ACKNOWLEDGMENTS

First and foremost, I thank my advisor Dr. Rowena Lohman, who has supported me during my past three years here at Cornell University. I began as a field geologist who had no coding skills and only the most vague comprehension of InSAR, and have emerged on the other side with a wealth of knowledge. She has always counseled me to push my boundaries past my comfort level and, as a consequence, she has helped me to use my time at Cornell in an amazingly efficient manner. Her guidance in research has been invaluable. I enter the next phase of my academic life stronger and more confident due to her influence.

Many thanks as well to my other committee members, Dr. Richard Allmendinger and Dr. Christopher Earls. Aside from his formal Structural Geology class, Rick was kind enough to offer an in-depth independent study experience that gave me additional access to his formidable knowledge of structural geology, an experience I will carry with me for years to come. Chris has provided a great deal of support as I continue to discover my research interests and plot the next chapter of my education. His interest in my research always inspires confidence. I am grateful to have been able to work with such excellent mentors during my time here at Cornell.

I would also like to thank Dr. Christopher Andronicos, who served as a member of my committee before his departure from Cornell. Chris's guidance and his faith in my abilities helped me enormously during my first year at Cornell.

I have been fortunate to be a member of an extremely supportive lab group. Bill Barnhart, Phil Nee, Chelsea Scott, and Francisco Delgado: thank you for sharing your lab space and expertise. To Scott Henderson, Andrew Melkonian, Jennifer Jay, and Holly

Taylor: thank you for your help and your friendship. Special thanks in particular to Andrew Melkonian and Jennifer Jay, who have never turned down an opportunity to help if they could, and without whom my knowledge of the Generic Mapping Toolbox would be significantly reduced. Thank you also to Dr. Julie Elliott, who read the first draft of the introduction to this thesis, and whose comments guided it's structure to a much better place than where it began.

Many heartfelt thanks to Dr. Muawia Barazangi for your kindness and guidance over the last three years. Muawia has seen to it that my scientific method has met a satisfactory standard, and his grading system has motivated my productivity (as have unexpected afternoon snacks).

Thanks as well to George Hade for your invaluable guidance when dealing with the seismometer, as well as your afternoon chats. Chen Chen (CC) and Diego Quiros have never balked at an opportunity to assist me with any questions I had about running the seismometer station, and I'm sure they have prevented more than one fire during smoke paper preparation.

I owe an enormous debt of gratitude to the administrative staff of Snee Hall; I don't think I'm able to count the number of times I have come to Savannah Sawyer, Amy Colvin, and Judy Starr for help and guidance.

My thanks go out to the participants of the weekly Andes Seminar, which I've found to be one of the most enlightening experiences during my time at Cornell. To everyone who has ever attended one of my seminars: thank you for providing feedback, and for doing your best to stay awake on a Friday afternoon.

I am grateful for the friends I've made during my time here at Cornell, especially Elaina Shope, Erin and Josh Meyer-Gutbrod, Tim Reber, Nicolas Cosentino, Caitlin Cox, Alex Mellnik, Felipe Aron, Mary Kosloski, and Brita Lorentzen, all of whom have been at the center of many of my fondest memories during my time here.

Koenraad Beckers has seen me through the good and occasionally frustrating times of my research here at Cornell, and I don't think I would've fared half as well without his support. I look forward to many years of visits (and miles!), and the kindness I've come to know and appreciate.

Last and certainly not least, I thank my parents for their unwavering support during these exciting years.

I was supported during my time at Cornell by NASA grant NNX10AQ80G. Data used in this thesis was acquired from the Japanese Aerospace Exploration Agency by NASA and is available through the Alaska Satellite Facility.

TABLE OF CONTENTS

LIST OF FIGURES

LIST OF TABLES

CHAPTER 1

INTRODUCTION

1.1 Motivation

Over the past few decades, interferometric synthetic aperture radar (InSAR) has emerged as a valuable tool for studying crustal deformation signals [*Zebker and Villasenor*, 1992; *Bürgmann et al.*, 2000; *Hanssen*, 2001; *Pritchard*, 2006; *Rott*, 2009]. Its applications to studies of tectonic and non-tectonic sources are varied, including earthquakes and fault-related processes [e.g., *Massonnet et al.*, 1993; *Fialko et al.*, 2001; *Elliott et al.*, 2008; *Lohman and Barnhart*, 2010], volcanic deformation [e.g., *Wicks et al.*, 2006; *Henderson and Pritchard*, 2013], vegetation structure [e.g., *Hagberg et al.*, 1995; *Cloude and Papathanassiou*, 1998; *Balzter*, 2001; *Kellndorfer et al.*, 2004; *Treuhaft et al.*, 2004], and anthropogenic signals [e.g., *Amelung et al.*, 1999; *Finnegan et al.*, 2008].

In addition to studies of crustal deformation, InSAR is also used to generate digital elevation models (DEMs) [e.g., *Graham*, 1974; *Zebker and Goldstein*, 1986; *Bürgmann et al.*, 2000; *Hanssen*, 2001], the most notable example being the products of the Shuttle Radar Topography Mission (SRTM) [*Farr et al.*, 2007]. While much of the focus of InSAR research in recent years has been on deformation, changes in the elevation of the ground surface can be of great scientific or societal interest as well. Examples include elevation and volume change due to anthropogenic processes such as open-pit mining operations, and natural processes such as glacier thinning or terrain alteration resulting from effusive volcanic eruptions [*Bombrun et al.*, 2009; *Herrera et al.*, 2010; *Ebmeier et al.*, 2012]. This thesis describes two previously undocumented elevation change signals observed in the Pacific Northwest that are of anthropogenic

origin. In the second chapter of this thesis, a proxy for canopy height determined using interferometric phase differences between adjacent logged and forested regions is presented. The third chapter determines estimates of the amount of material displaced during mining operations at the Centralia Coal Mine in Centralia, Washington.

Quantifying the amount of surface change due to anthropogenic activities is not only critical for tracking the altering landscape of the Pacific Northwest and reducing the observed error in interferograms attributable to elevation change. Deforestation is one of the most significant contributors to global carbon emissions, and quantifying changes in vegetation structure can assist in efforts to monitor and mitigate the effects of deforestation on climate change. Similarly, mining operations can have a lasting impact on surrounding communities due to triggered seismicity, landslides, and groundwater disruption or contamination. By monitoring mining operations, areas of hazard can be identified and the potential impacts on surrounding regions mitigated.

1.2 Interferometric Synthetic Aperture Radar (InSAR)

InSAR studies may be undertaken using either airplane- or satellite-based platforms, and can be performed as single- or repeat-pass surveys [*Bürgmann et al.*, 2000; *Hanssen*, 2001]. With repeat-pass InSAR, the method employed in this thesis, an airplane- or satellite-based sensor passes over the ground at two different times, transmitting a radar signal and recording the backscattered phase and amplitude information of the return reflected from the ground at each pass (Figure 1.1). Each pixel of a SAR acquisition is located in the resulting image as a function of azimuth (location along flight path) and range (location perpendicular to flight path). The amplitude of a

SAR image is sensitive to the reflective strength of scatterers within a pixel, which is a function of surface roughness and dielectric properties [*Bürgmann et al.*, 2000; *Pritchard*, 2006]. The radar signal propagates a distance of many millions of full cycles as it travels between the satellite and the ground and back, but the receiver is only able to record the phase to within a fraction of a cycle [*Bürgmann et al.*, 2000; *Hanssen*, 2001].

Some studies rely on a single SAR acquisition and utilize only the amplitude of the backscattered signal to determine ground properties such as soil moisture, vegetation characteristics, and surface roughness over water [*Bürgmann et al.*, 2000; *Rosen et al.*, 2000]. The phase value of individual pixels is random due to the large size of pixels (~20m) relative to the size of the randomly ordered scatterers (few cm), so phase information from individual SAR images has little meaning. However, if the individual scatterers do not move significantly between acquisitions, the random phase field varies in a coherent manner from image to image. SAR interferometry makes use of the phase information of each pixel by combining two co-registered SAR images through multiplication of one SAR image by the complex conjugate of the other [*Bürgmann et al.*, 2000; *Hanssen*, 2001; *Rott*, 2009]. The phase value of the interferometric product, called an interferogram, is the sum of various influences of the ground on the backscattered signal, including deformation of the ground surface, topography, and noise sources such as errors in the estimation of the satellite's orbit, atmospheric water vapor, and soil moisture [*Bürgmann et al.*, 2000; *Rosen et al.*, 2000; *Hanssen*, 2001; *Rott*, 2009].

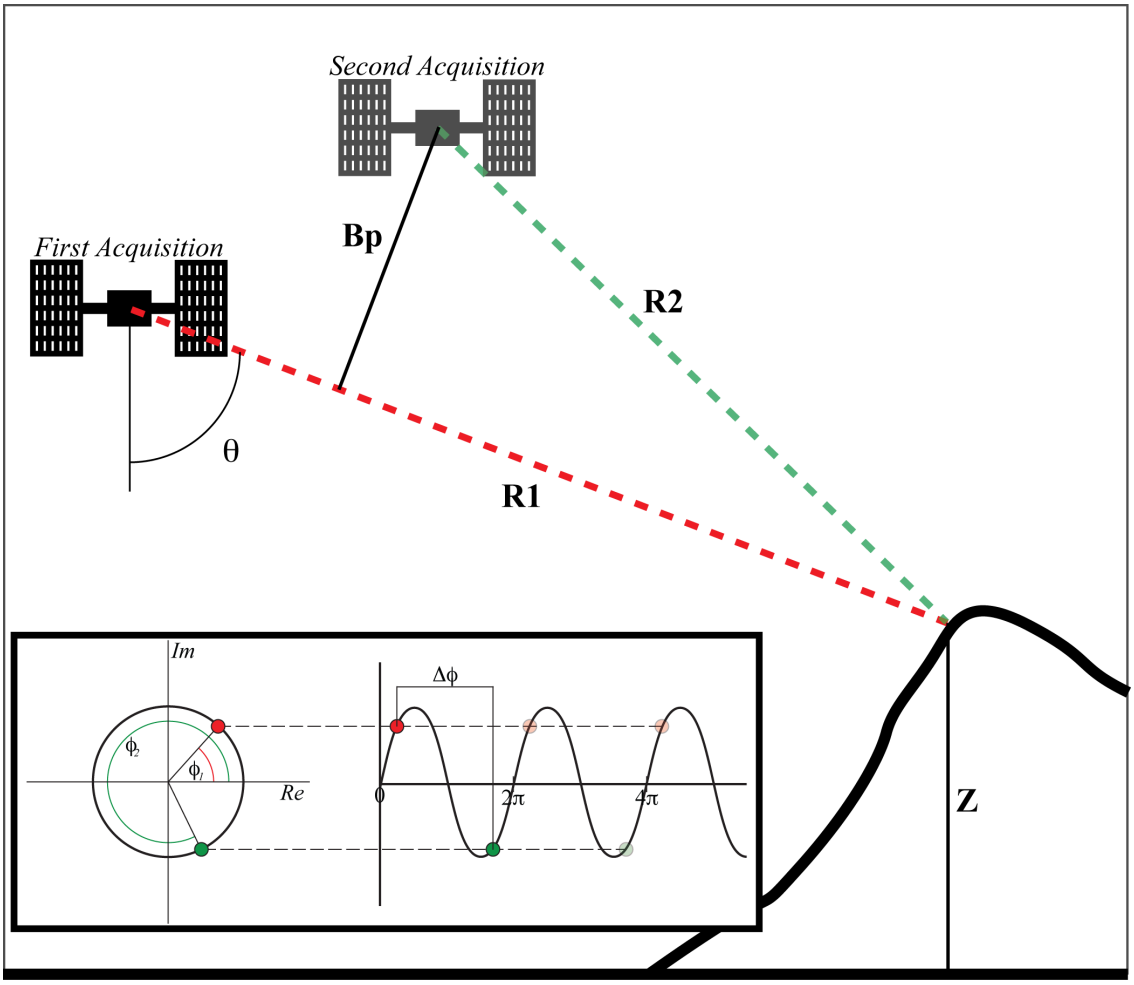

Figure 1.1: Conceptual diagram of a repeat-pass SAR survey. The satellite passes over the region of interest at two times, acquiring two SAR images of the ground surface. R1 and R2 indicate the range (distance from the ground to the satellite) of the two surveys; θ is the look angle of the sensor, measured from nadir; Bp is the perpendicular baseline, or spatial separation between the satellite's position at the time of each acquisition; and Z indicates the height of a pixel within the SAR image. Inset is a conceptual diagram of the phase of the pixel during each of the two passes. The red dot (ϕ_1) indicates the phase value of the pixel at the time of the first acquisition; the green dot (ϕ_2) indicates the phase value at the time of the second acquisition; $\Delta\phi$ is the difference in phase of the pixel between the first and second acquisitions. Transparent dots represent the inherent 2π ambiguity of the signal.

1.3 Baseline-dependent Signals

Signals observed in interferograms can be divided into two categories: those that exhibit a strong time dependence, and those that have no time dependence but instead are correlated with the separation between the sensors at the time of image acquisition, known as the perpendicular baseline (Bp, Figure 1.1). Time-variable signals are often the result of processes that are of interest to the scientific community, such as volcanic deformation, anthropogenic withdrawal of subsurface fluids, and earthquakes, which has resulted in a wide range of algorithms for extracting and interpreting them [e.g., *Berardino et al.*, 2002; *Hetland et al.*, 2012; *Agram et al.*, 2013]. Signals dependent on perpendicular baseline are the result of topographic variation [*Bürgmann et al.*, 2000; *Rosen et al.*, 2000; *Hanssen*, 2001; *Rott*, 2009].

As mentioned above, the only factor contributing to the interferometric phase that is baseline-dependent is the effect of topographic relief, and DEMs can be generated using pairs of interferograms with short time intervals (ideally acquired simultaneously) and long baselines [*Farr et al.*, 2007]. As a result of the contribution of topographic relief to interferometric phase, errors in the DEM used to correct for the effects of topography will propagate into errors in the observed interferometric phase. Most algorithms that extract deformation histories from InSAR time series include a step where the baseline-dependent component of the signal is solved for and characterized as a DEM error [e.g., *Berardino et al.*, 2002]. However, the baseline-dependent component itself is not typically a target of research [e.g., *Fisher and Tate*, 2006; *Bombrun et al.*, 2009; *Ebmeier et al.*, 2012]. As discussed in section 1.1, this thesis exploits the baseline-dependence of

signals associated with logging and mining operations in the Pacific Northwest to quantify the effect of these anthropogenic activities on observed surface changes.

1.4 Outline of Thesis

Chapter 2 focuses on a baseline-dependent signal associated with a specific type of logging known as clearcutting commonly practiced throughout the Pacific Northwest. This style of logging involves the removal of all trees within a particular plot of land. We observe phase differences between adjacent cleared and forested regions that are baseline-dependent. This signal is not associated with an error in the DEM estimate of elevation of the ground surface, but is instead a true difference in height between the scattering elements comprising the vegetated and cleared regions. We use the observed relationship between perpendicular baseline and this phase difference to calculate the height of the scattering elements within the vegetated regions. Because of the long wavelength of the radar used (23.6 cm), the dominant scattering elements are not located at the top of the trees but represent a volume deeper within the vegetation. We present a map of the height of the scattering elements within the forests of the Pacific Northwest, which can be related to canopy height. We find that the height of the characteristic scatterers determined using our methods are ~50% shorter than canopy heights determined using Light Detection and Ranging (LiDAR), another commonly employed remote sensing method for determining regional canopy height. This difference is consistent with the results of previous studies that compared inferred canopy height using remote sensing at different wavelengths [*Sarabandi and Lin*, 2000; *Balzter et al.*, 2007; *Andersen et al.*, 2008; *Breidenbach et al.*, 2008].

Chapter 3 focuses on a signal caused by massive transport of material near the Centralia Power Plant and adjacent mine in Centralia, Washington. Unlike the signal discussed in Chapter 2, this baseline-dependent signal can be attributed to changes in the actual elevation of the ground surface over time. In this locality, large-scale operations have moved millions of cubic meters of material. We use the catalog of InSAR data, combined with two independent DEMs generated at different times in the past, to determine the historical pattern of material transport and an estimate for the volume of material displaced in the region.

CHAPTER 2

DETERMINING CANOPY HEIGHT IN THE PACIFIC NORTHWEST

2.1 Introduction

2.1.1 Deforestation and Climate Change

The Food and Agriculture Organization (FAO) of the United Nations estimates that, as of 2012, forests account for approximately 30% of global land cover [*Food and Agriculture Organization of the United Nations*, 2012]. Since 1800, approximately 1 billion hectares of the World's land has been deforested, with as much as half of this loss occurring since 1950 [*Williams*, 2003; *Food and Agriculture Organization of the United Nations*, 2012]. Anthropogenic deforestation occurs primarily as a result of conversion of forested land to agricultural uses through methods such as "slash-and-burn," though harvesting of forests for timber is also a significant factor [*Food and Agriculture Organization of the United Nations*, 2010]. Between 2000 and 2010, net losses of forests were approximately 5.2 million hectares per year, down from approximately 8.3 million hectares per year between 1990 and 2000 [*Food and Agriculture Organization of the United Nations*, 2010]. While many regions have reported net afforestation in recent years, the annual rate of deforestation between 2000 and 2010 still amounts to a loss of forest equal in area to a region the size of Costa Rica [*Food and Agriculture Organization of the United Nations*, 2010].

The contribution of this ongoing global deforestation to climate change has been of increasing concern over the past few decades. An estimated 650 billion metric tons of carbon are stored in forests globally, more than is contained in the atmosphere [*Food and Agriculture Organization of the United Nations*, 2010]. Carbon emissions due to

deforestation occur through the combustion of forest mass, either through burning of forests or timber production, as well as through the decomposition of remaining material [*van der Werf et al.*, 2009]. The 2007 Intergovernmental Panel on Climate Change (IPCC) report states that approximately 17.3% of anthropogenic greenhouse gas emissions can be attributed to CO_2 emitted as a result of deforestation. This proportion of greenhouse gas emissions is second only to emissions due to fossil fuel use [*Intergovernmental Panel on Climate Change*, 2007]. Estimates of the contribution of deforestation to greenhouse gas emissions since the IPCC 2007 report have revised this number downwards to approximately 12%; however, the impact of deforestation on total anthropogenic carbon emissions remains significant [*van der Werf et al.*, 2009].

Any legislation that seeks to curb deforestation rates must be accompanied by a means for verifying compliance and taking inventories of current forest stocks. Such inventories also allow for assessment of the efficacy of forest management practices and monitoring of overall forest health. Currently, many of the statistics on global forest change depend on the self-reporting of nations, making them subject to the ability and desire of a nation to accurately report on its forest inventory [*Food and Agriculture Organization of the United Nations*, 2010]. These inventories are typically undertaken through comprehensive ground surveys or remote sensing methods. Vegetation structure and canopy height are two parameters of interest when assessing a forest inventory, and can be combined with allometric relationships to determine the biomass and, in turn, carbon stock of a forested region [e.g., *Goetz et al.*, 2009; *Solberg et al.*, 2010; *Sandberg et al.*, 2011; *Lynch et al.*, 2013].

We introduce a method for determining regional canopy height of forests that have experienced clearcutting through the use of satellite-based interferograms, with an application to the Pacific Northwest. Given sufficient data availability, this approach could easily be applied to forests globally.

2.1.2 Monitoring global deforestation

Before the advent of remote sensing technologies, ground surveys were the primary method for assessing forest inventories. Ground surveys on a local scale are cost-efficient and allow for measurements and observations of forest characteristics such as species diversity, overall health, and forest density to be made with relative ease; however, ground surveys with the repeat times necessary to verify compliance with legislation or to assess the efficacy of new forest management practices require a great deal of time and human labor and, for logistical and political reasons, are difficult to perform in many forested regions [*Kovats*, 1997; *Gatziolis et al.*, 2010]. In light of these challenges, remote sensing methods that can be conducted at a global scale with frequent repeat intervals can serve as a powerful complement to ground surveys [*Lynch et al.*, 2013] .

One of the most frequently used remote sensing methods for monitoring forests, particularly for the determination of canopy height, is light detection and ranging (LiDAR), also known as airborne laser scanning (ALS) (Figure 2.1). Numerous studies have investigated the capabilities of LiDAR to determine forest characteristics such as vegetation density, structure, and canopy height [e.g., *Andersen et al.*, 2004; *Balzter et al.*, 2007; *Sexton et al.*, 2009; *Lefsky*, 2010]. These studies suggest that canopy height

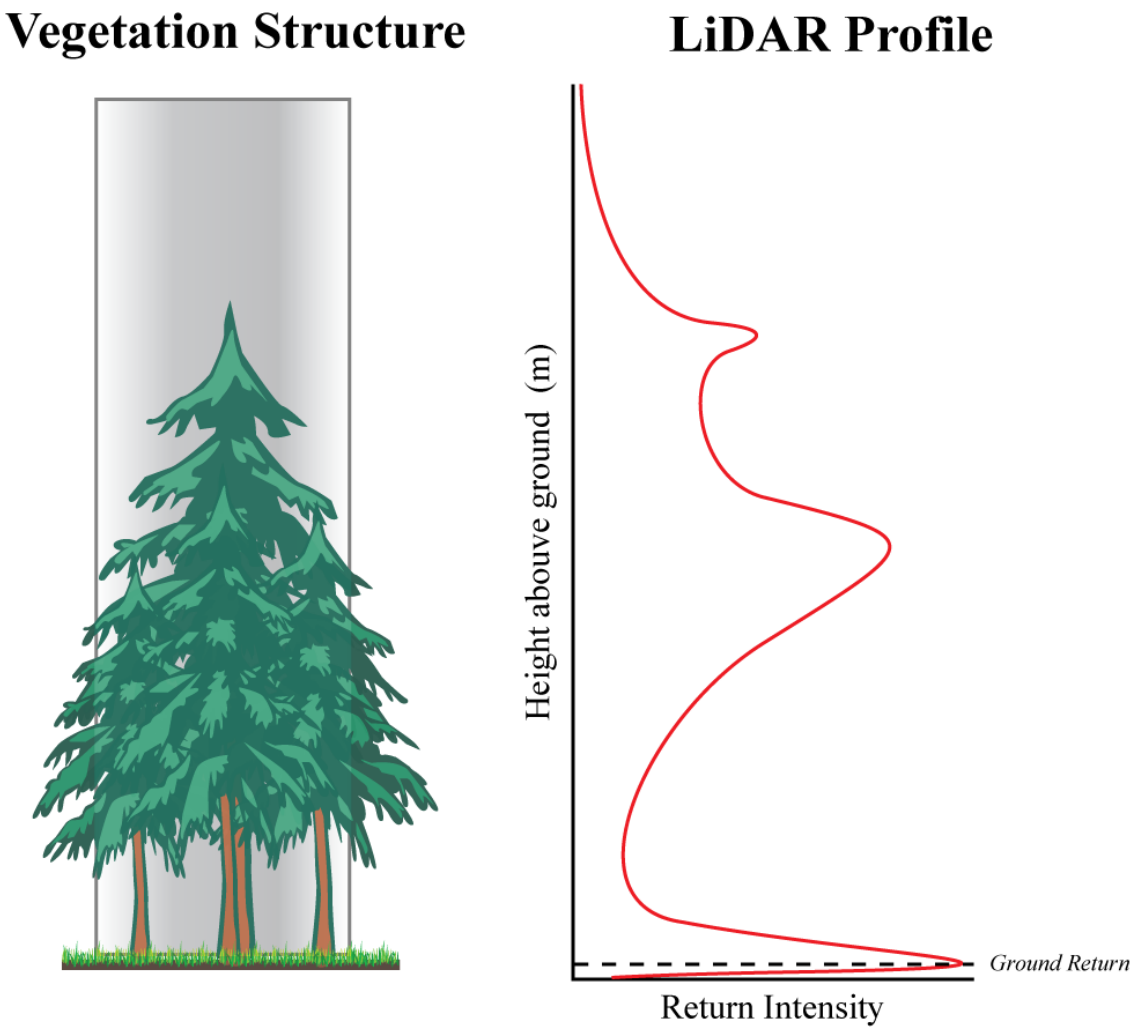

Figure 2.1: Schematic diagram of a LiDAR survey. A tree stand in the path of the LiDAR beam is depicted on the left; a profile of returns from the surveyed forest is depicted at right. The ground return is the strongest return; returns from within the canopy provide estimates of vegetation structure.

within the footprint of the LiDAR beam can be measured with centimeter-scale accuracy. A global canopy height map produced using Moderate Resolution Imaging Spectroradiometer (MODIS) and Geoscience Laser Altimeter System (GLAS) data indicates that canopy heights in the Pacific Northwest are among the tallest in the world, with many regions consisting of 35-65 meter tall trees [*Lefsky*, 2010]. Both satellite- and airplane-based platforms are capable of frequent repeat LiDAR measurements, potentially on global scales [*Treuhaft et al.*, 2004]. However, satellite-based platforms average measurements over beam footprints that can be tens of meters in diameter, with acquisitions separated by hundreds of meters along track, and airborne platforms are prohibitively expensive to use on a global scale [*Schutz et al.*, 2005]. LiDAR systems are also hampered by cloud cover and steep slopes, both of which are frequent conditions in many forested regions of interest [*Baltsavias*, 1999; *Asner et al.*, 2005; *Gatziolis et al.*, 2010].

Synthetic aperture radar (SAR) is another remote sensing tool that can place constraints on vegetation characteristics, particularly since active imaging at microwave wavelengths is possible at night and in regions with dense cloud cover [e.g., *Treuhaft et al.*, 2004](see Figure 1.1). Previous studies have investigated the feasibility of using the amplitude of the backscattered signal from SAR images as well as the coherence and/or phase information from pairs of images as a proxy for biomass and vegetation structure, particularly when data from multiple polarizations is available [e.g., *Dobson et al.*, 1992, 1995; *Hagberg et al.*, 1995; *Treuhaft et al.*, 1996; *Askne et al.*, 1997; *Wegmuller and Werner*, 1997; *Cloude and Papathanassiou*, 1998; *Mercer*, 2001; *Balzter et al.*, 2007; *Walker et al.*, 2007; *Breidenbach et al.*, 2008]. Other groups have compared bare-earth

digital elevation models (DEMs) with the elevation product produced by the Shuttle Radar Topography Mission's (SRTM) C-band radar sensor to determine canopy height [e.g., *Kellndorfer et al.*, 2004]. Satellite-based SAR systems generate images that are ~100km x 100km in scale with pixels on the order of a few tens of meters or smaller [*Bürgmann et al.*, 2000; *Hanssen*, 2001]. The repeat intervals for SAR satellites range from days to months – 42 days in the case of the Japanese Aerospace Exploration Agency's (JAXA) Advanced Land Observation Satellite (ALOS) used in this study – allowing for frequent repeat observations of forest properties [*Igarashi*, 2001].

In this chapter we present an algorithm for determining regional canopy height using single-polarization ALOS data covering the Pacific Northwest, one of the largest temperate forests in the world in terms of forest area and canopy height [*Alaback*, 1991; *DellaSala*, 2011]. Our methods make use of observed interferometric phase differences between adjacent cleared and forested regions within this study area.

2.2 Methods

2.2.1 Data

We use Phased Array type L-band Synthetic Aperture Radar (PALSAR) (λ = 23.6 cm) data collected by ALOS between January 1, 2007 and March of 2011 (Figure 2.2). The number of available acquisition dates varies between frames across our study area (Appendix A). We generate interferograms using the Repeat Orbit Interferometry PACkage (ROI_PAC), an open-source software package for processing SAR acquisitions, developed jointly by the Jet Propulsion Laboratory (JPL) and Caltech [*Rosen et al.*, 2004b]. Interferograms were downsampled 12 times in the azimuth

direction and 4 times in the range direction, but no other averaging or filtering was applied.

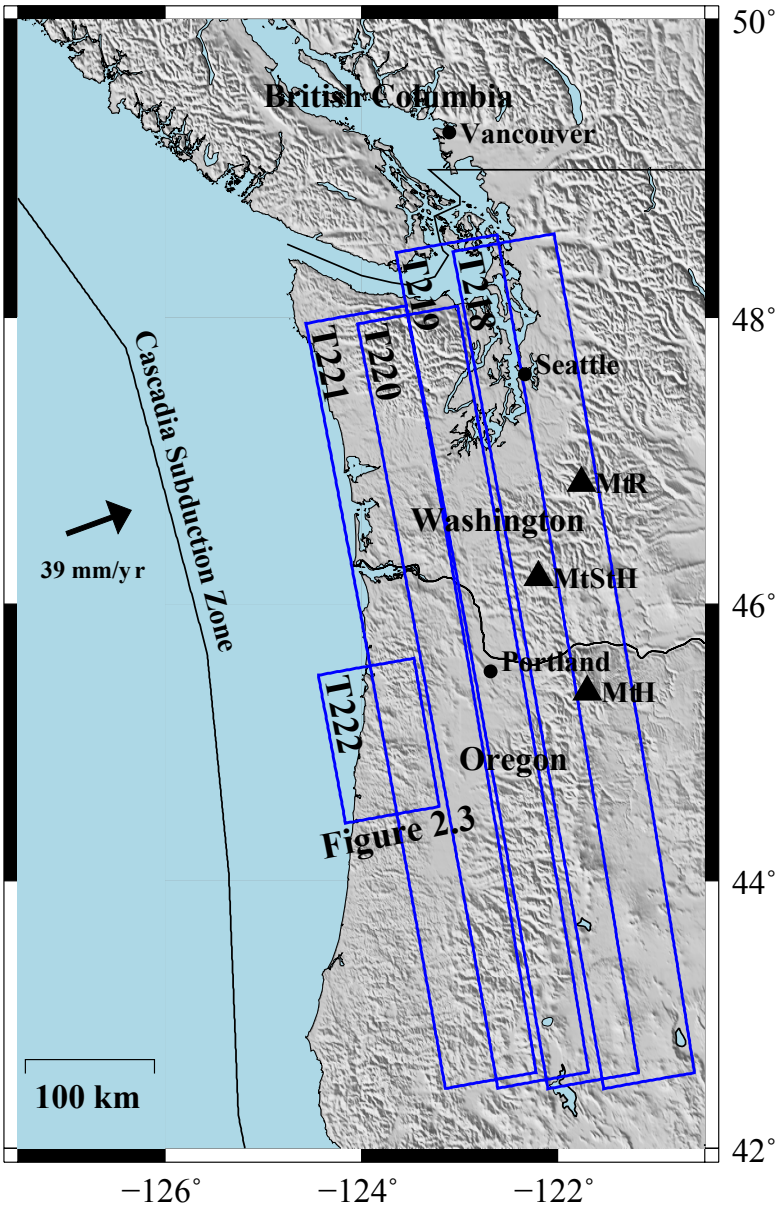

Figure 2.2: Pacific Northwest, with coverage of SAR imagery used in this study (boxes) and location of Figure 2.3. Arrow indicates convergence between Juan De Fuca and North American Plates at the Cascadia Subduction Zone. MtR – Mt. Rainier; MtStH – Mt St. Helens; MtH – Mt. Hood.

Interferometric processing for the purpose of deformation or vegetation studies requires removal of the effects of topography from the interferogram, usually in the form of a digital elevation model (DEM). We use the 1 arc-second National Elevation Dataset (NED) product, the primary source of elevation data produced by the USGS [*Gesch et al.*, 2002; *Maune*, 2007]. The NED is a bare-earth elevation product, updated bimonthly to integrate new elevation datasets as they become available.

For each frame, we generate all interferograms with perpendicular baselines <2500 m and temporal baselines <~1 year (Appendix A). We rectify all interferograms to a common grid in radar coordinates before further processing.

2.2.2 Description of phase signal attributed to variations in canopy height

An example interferogram covering a short, 46-day time interval is shown in Figure 2.3. The large spatial scale signals can likely be attributed to variations in atmospheric water vapor and/or inaccuracies in our knowledge of the satellite location at the two acquisition times. Also apparent are small, quasi-rectangular regions of coherent variations in the interferometric phase. We attribute these phase variations to the clearing of forests due to timber production, verified through comparisons with optical imagery (Figure 2.3b,c). Interferograms spanning a time period where forest is cleared are decorrelated within those regions but coherent during periods of no disturbance (Figure 2.4).

Interferometric phase is a function of many variables, including deformation of the ground surface, changes in the dielectric constant from variations in soil moisture,

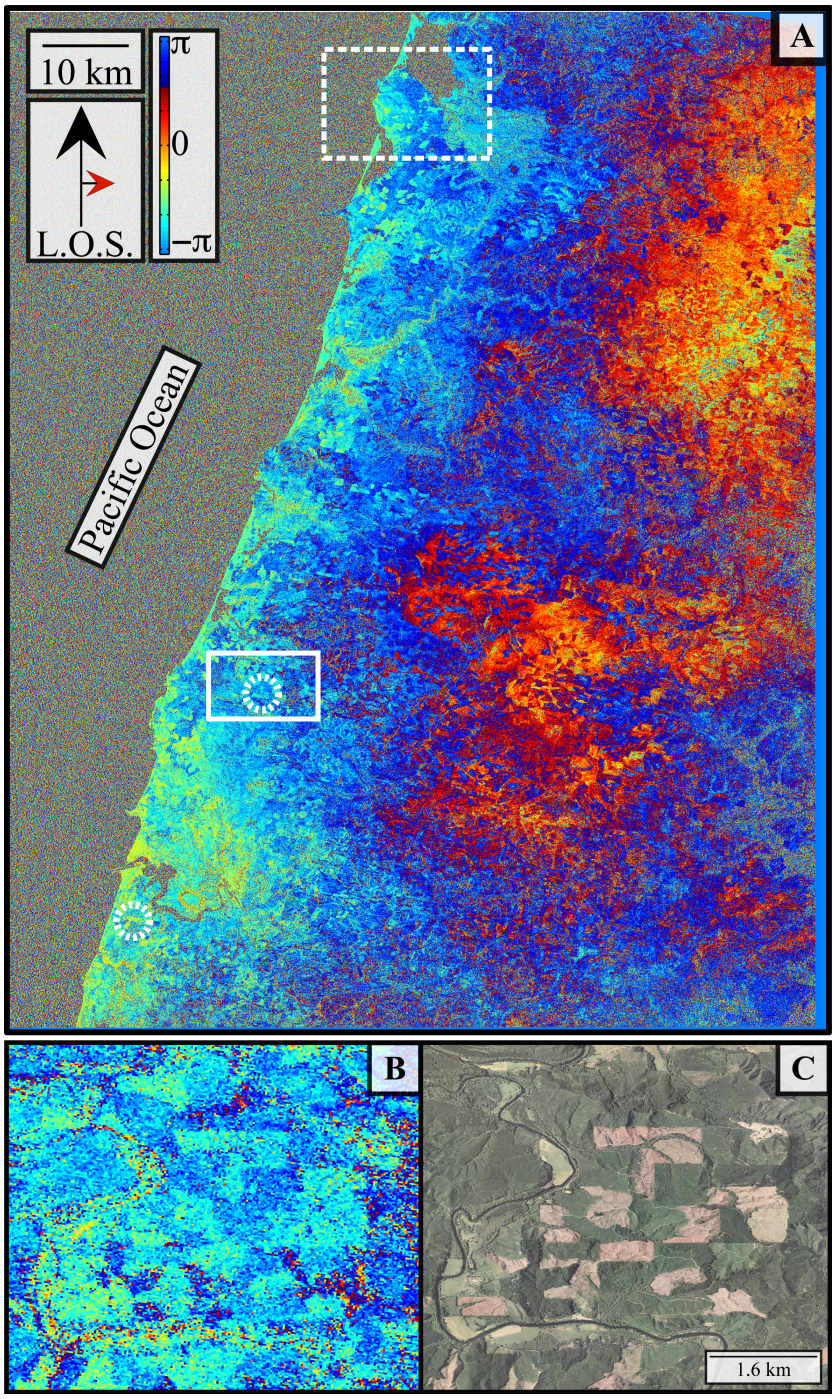

Figure 2.3: (a) Example wrapped interferogram (path 222, frame 890), spanning 7/18/2009 – 9/2/2009, perpendicular baseline of 470m. Scale bar is in radians. White solid line indicates location of (b) and (c). White dashed line indicates approximate extent of Figures 2.4 and 2.7. White dashed circles indicate locations of the two cleared regions examined in Figures 2.9 and 2.12. Arrows indicate satellite line-of-sight (red) and travel (black) directions. Comparison of interferogram (b) with optical imagery (c) confirms correlation of quasi-rectangular phase signals with clearing of forests. Optical imagery collected during the summer of 2005 and made available through Oregon Explorer (*http://oregonexplorer.info*).

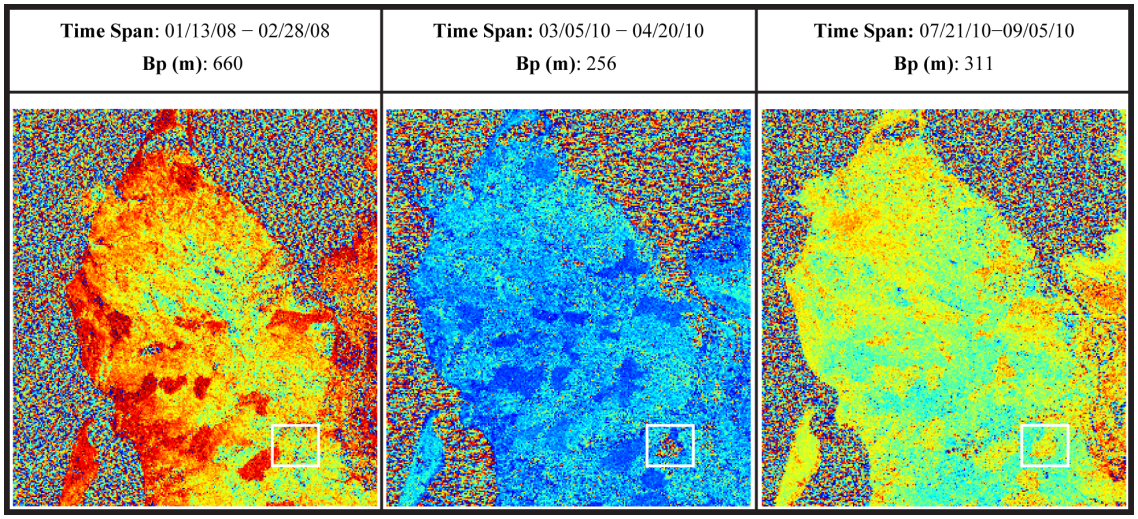

Figure 2.4: Three interferograms covering the boxed region in Figure 2.3. The white outlined area indicates a region cleared between March 5, 2010 and April 20, 2010. (a) Regions that are forested appear light green and yellow. Cleared regions appear red. The region outlined by the white box appears light green and yellow, indicating that it was forested at this time in 2008. (b) The same region outlined by the white box is decorrelated due to clearing of the forested area during that time span, much as harvested crops might appear. (c) In the third interferogram, the region outlined by the white box now exhibits the same phase signature (yellow instead of light blue-green) as surrounding cleared regions. The appearance of the cleared area is confirmed in our mask products (Figure 2.7).

delays due to radar propagation within the atmosphere, and errors in the DEM used during analysis [e.g., *Bürgmann et al.*, 2000]. The key characteristic linking the observed phase differences between cleared and forested areas to canopy height is that the difference in phase increases linearly with the perpendicular baseline separating the two satellites at the time of image acquisition (Figure 2.5). This suggests that the signal is due to differences in elevation, as none of the other factors affecting interferometric phase should be correlated with baseline.

By design, the bare-earth NED DEM used in our processing of the interferograms does not contain trees. Therefore, we attribute our observed phase differences between adjacent cleared and forested regions to differences in the elevation of the effective L-band phase center of each pixel due to the varying height of trees and other vegetation.

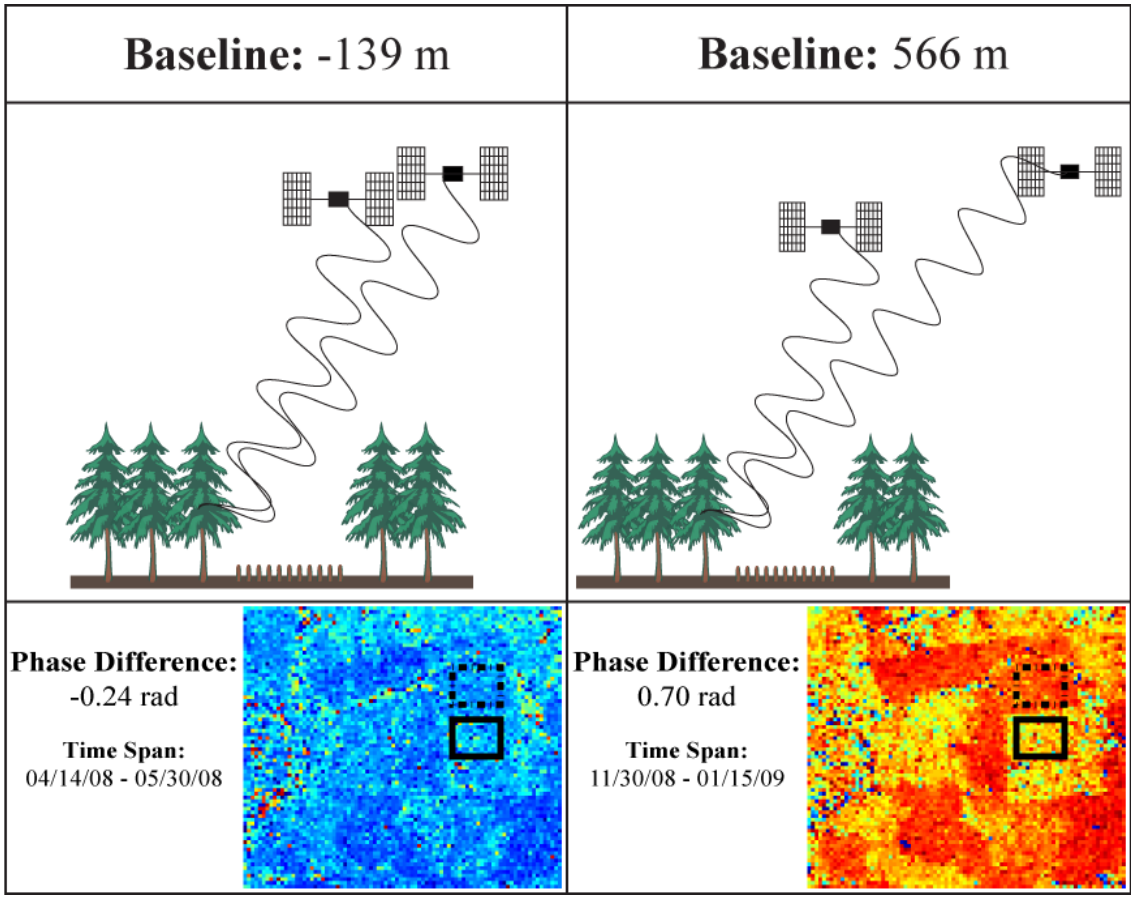

Figure 2.5: Schematic drawing of increased difference in phase with increasing baseline. The two satellites in each panel represent the two acquisitions used to generate the interferogram. For our study, the two satellites represent the two passes of ALOS over the region of interest at two different times. Unlike deformation signals, the phase differences observed due to clearing are not due to changes in the properties of the scatterers between the first and second acquisition. Observed phase differences are due to the difference in height between the bare ground where a clearing has occurred and the standing forests that surround it. The value of the phase difference increases with increasing baseline. For a small baseline interferogram such as the one shown on the left, the signal of the cleared region is barely visible. The difference in phase between pixels within the cleared region (dotted box) and pixels within the standing forest (solid box) is small. An interferogram with a larger perpendicular baseline shows a more pronounced signal, and the difference in mean phase between the forested and cleared regions increases as well.

The slope of the relationship between phase change and baseline for a set of interferograms can be used as a proxy for forest canopy height. L-band radar does not interact with the very top of the canopy, so we expect the apparent heights to be lower than those obtained in the field, from LiDAR data, or by using C-band or X-band SAR sensors (Figure 2.6). The scattering phase center for a given sensor and location will vary depending on factors such as forest density, canopy morphology, wavelength, and incident angle of the sensor [*Sarabandi and Lin*, 2000; *Izzawati et al.*, 2006; *Balzter et al.*, 2007; *Andersen et al.*, 2008; *Breidenbach et al.*, 2008].

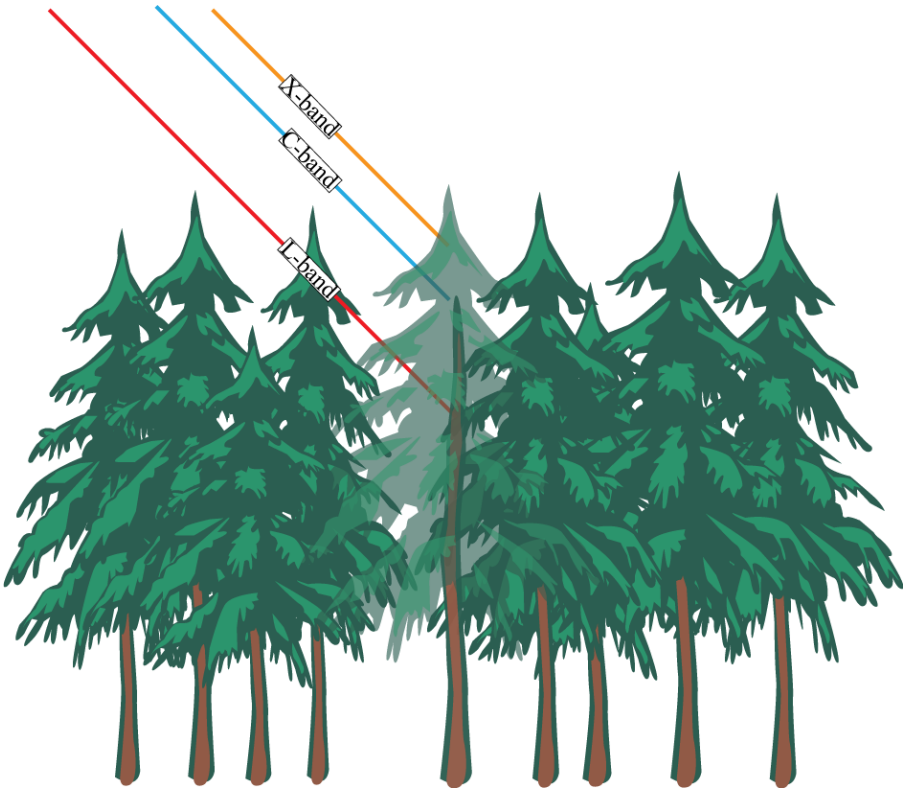

Figure 2.6: Schematic diagram comparing interaction depths of X-, C-, and L-band radar sensors in a dense forest stand. TerraSAR-X, the German Aerospace Center's (DLR) X-band satellite, operates at a wavelength of 3.1 cm; a C-band sensor, such as the European Space Agency's (ESA) European Remote Sensing (ERS) satellites, operates at a wavelength of 5.6 cm; the L-band sensor aboard ALOS operated at a wavelength of 23.6 cm. With increasing wavelength, it is expected that the height of the observed scattering phase center will decrease, as depicted in this schematic.

2.2.3 Automated identification of cleared regions

The larger scale features (>10 km) in each interferogram are likely due to variations in atmospheric properties between the times of image acquisition and errors in the estimates of satellite position (see Figure 2.3). Therefore, we are interested only in the variations in phase at the shortest spatial scales, across boundaries between forested and cleared regions. Focusing on phase differences across such small distances removes the need to consider these other sources of error.

As illustrated in Figures 2.3, 2.4, and 2.5, bare regions where clearcutting has occurred are visually apparent in interferograms as quasi-rectangular regions with a phase value that differs from surrounding pixels. However, isolating these cleared regions by hand for all interferograms spanning a region as large as the Pacific Northwest would be prohibitively expensive. Instead, we use a combination of several other publicly available remote sensing datasets to automate generation of subsets of each interferogram that we characterize as "forested", "bare" or "unclassified". Because many regions were cleared during the timespan of the available SAR data, we included a time-variable component that ensured that we were not averaging tree heights over a time interval during which logging had occurred.

2.2.4 Initial classification: NLCD2006 Dataset

For an initial, coarse classification, we use the National Land Cover Database 2006 (NLCD2006) land cover product [*Fry et al.*, 2011; *Wickham et al.*, 2013]. The NLCD2006 land cover product is a wall-to-wall classification raster image (30 m pixels)

over the conterminous United States with 16 land cover classifications. The NLCD2006 dataset is derived from Landsat Enhanced Thematic Mapper (ETM+) imagery and made available by the Multi-Resolution Land Characteristics Consortium (*http://www.mrlc.gov*).

We transformed and interpolated the data to radar coordinates using ROI_PAC. For the purposes of the canopy height estimation, we divided the NLCD2006 data into forested (land classifications 41, 42 and 43) and bare pixels (classifications 31, 52 and 71). All other classes, including water bodies (11, 12), developed regions (21, 22, 23, 24), wetlands (90, 95), and planted/cultivated regions (81, 82), were characterized as "unclassified" and were not used in our analysis.

2.2.5 Use of Landsat data to constrain temporal evolution

Though the NLCD2006 product provides a base map for identifying and isolating regions that were cleared or forested in 2006, land cover does not remain static over the time span of our data. Harvesting of the forest continues in this region, resulting in new cleared areas, and previously cleared regions are concurrently experiencing regrowth. At the present time, a new NLCD database is scheduled for release approximately every 5 years, which does not provide the temporal resolution necessary for determinations of canopy height based on InSAR data that is often acquired on a monthly basis.

In order to characterize the temporal variability of land cover in our study area during the 2007 – 2011 time frame of our study, we supplement the NLCD2006 data with yearly Landsat 5 Thematic Mapper (LTM5) acquisitions covering the Pacific Northwest.

Cloud cover was restricted to less than 20%, and for each frame we used the least cloud and ice-covered acquisition available for that year (Appendix B).

We generate a map of bare regions, which includes cities, roads, and deforested areas, for each year using the ratio of LTM5 band 2 (visible, 0.52 – 0.60 μm), and band 7 (mid-infrared, 2.08 – 2.35 μm). Figure 2.7 illustrates the rapidly evolving landscape changes observed in path 222, frame 890. Other frames exhibit similar changes in land cover.

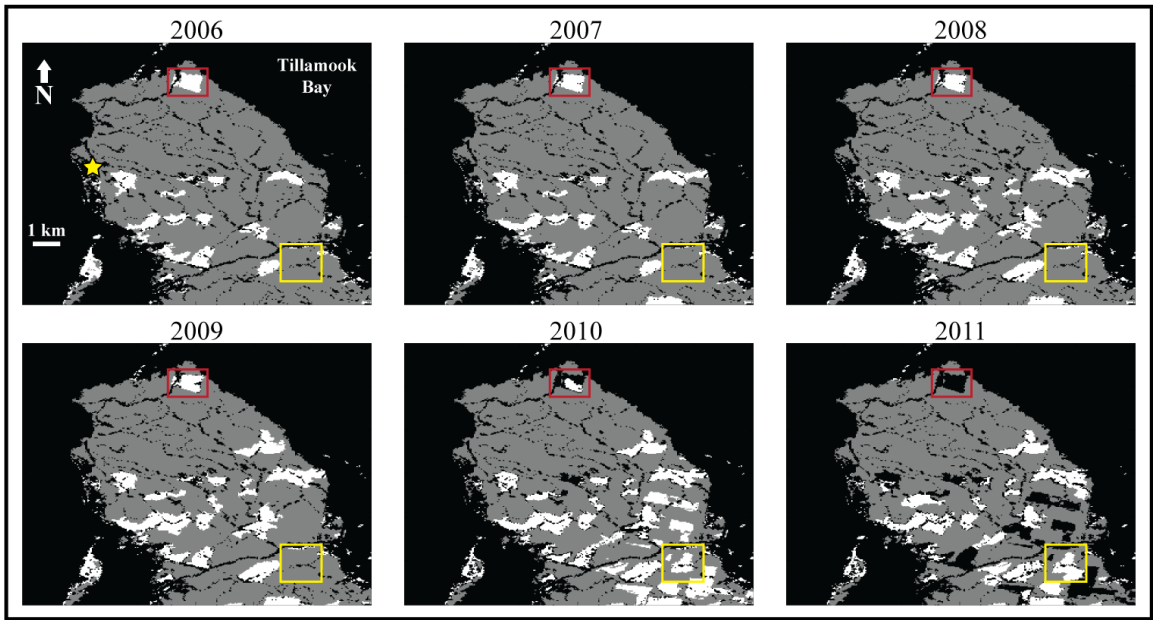

Figure 2.7: Six mask products covering boxed region indicated in Figure 2.3. Gray and white regions indicate forested and cleared areas, respectively. Black regions indicate areas that are not used in our canopy height estimation process, e.g., ocean, roads and waterways. Yellow star indicates location of Oceanside, OR. The number of clearcut regions increases markedly between 2006 and 2011, particularly in the southern portion of the masked region. The red box indicates a cleared area that experiences sufficient re-greening during the time span of our data that it is removed from our canopy height estimation process by 2011. The yellow box outlines the cleared area shown in Figure 2.4; note that it is converted from a forested to cleared region in 2010, verified in the interferogram examples above.

2.2.6 Canopy Height Estimation

We estimate canopy height with a running window of 40 x 40 pixels across each frame. At each location, we extract the average phase of pixels flagged as forested or cleared for each interferogram. The time-variable masks discussed above ensure that regions that were cleared during the time span of our interferogram set only contributed to the average "cleared" phase values after the clearing event. If the number of either forested or cleared pixels for a given interferogram within the running window is below a set threshold (50 pixels), that particular interferogram will not be included in the height estimation at that location. We determined the appropriate threshold based on how the variance in inferred canopy height changes with the number of pixels used. A height estimate is not included if fewer than 10 interferograms met our criteria at that location.

We determine the local phase changes between forested and bare regions by averaging the complex phase values in each area separately and then differencing them, also in the complex plane. Phase unwrapping – the process of converting the interferometric observations, which are "wrapped" from $-\pi$ to π, to the total amount of range change – carries with it many potential sources of error. This is particularly true for clearcut signals, since they have a sharp boundary across which it is not clear how many cycles of phase are represented (see Figure 1.1). Therefore, we estimate the average phase in each region using the full complex phase values at each pixel. One result of this approach is that our inferred phase change between clearcut and forested regions will also be wrapped, which has consequences described below in the discussion of inferred canopy heights. Each complex phase value Φ can be decomposed as:

$$\Phi = |\Phi| \exp(j\phi) \qquad \text{(Eq. 2.1)}$$

where $|\Phi|$ is the amplitude and ϕ is the phase. We normalize all values to unit amplitude and find the mean complex phase ($\overline{\Phi}$) of all pixels within the averaging region. If all pixels within the averaging region have approximately the same phase value, the magnitude of $\overline{\Phi}$ will be near unity – if the phase values are random, the magnitude will approach zero (Figure 2.8).

The variance of each estimate of average phase value for cleared and forested pixels is determined as:

$$\sigma^2 = -2(ln|\overline{\Phi}|) \quad \text{(Eq. 2.2)}$$

We determine ${\sigma_f}^2$ and ${\sigma_c}^2$ for forested and cleared pixel groups, respectively, with the total variance, ${\sigma_T}^2$, for phase differences being the sum of the variances of ${\sigma_f}^2$ and ${\sigma_c}^2$. The variance of each group of pixels is limited by the fact that phase values are restricted to the range -π to π. Above a level of $\sigma^2 \approx 0.6{\times}2\pi$, the phase values are essentially random. We remove all phase values where $\sigma^2 > 0.45{\times}2\pi$ from our analysis (see Figure 2.8).

Since our data is wrapped, the determination of canopy height at each location is nonlinear. The optimal slope, *m*, of the line (which goes through zero) relating phase changes to baseline will minimize a weighted error, E:

$$E = \|Gm - d\| \quad \text{(Eq. 2.3)}$$

where *G* is a 1 x *n* matrix of perpendicular baseline values for *n* interferograms and *d* is a 1 x *n* matrix of complex phase differences observed between cleared and bare regions. We weight *G* and *d* by the inverse of the data variances generated as described above. The phase center height associated with each value of *m* is:

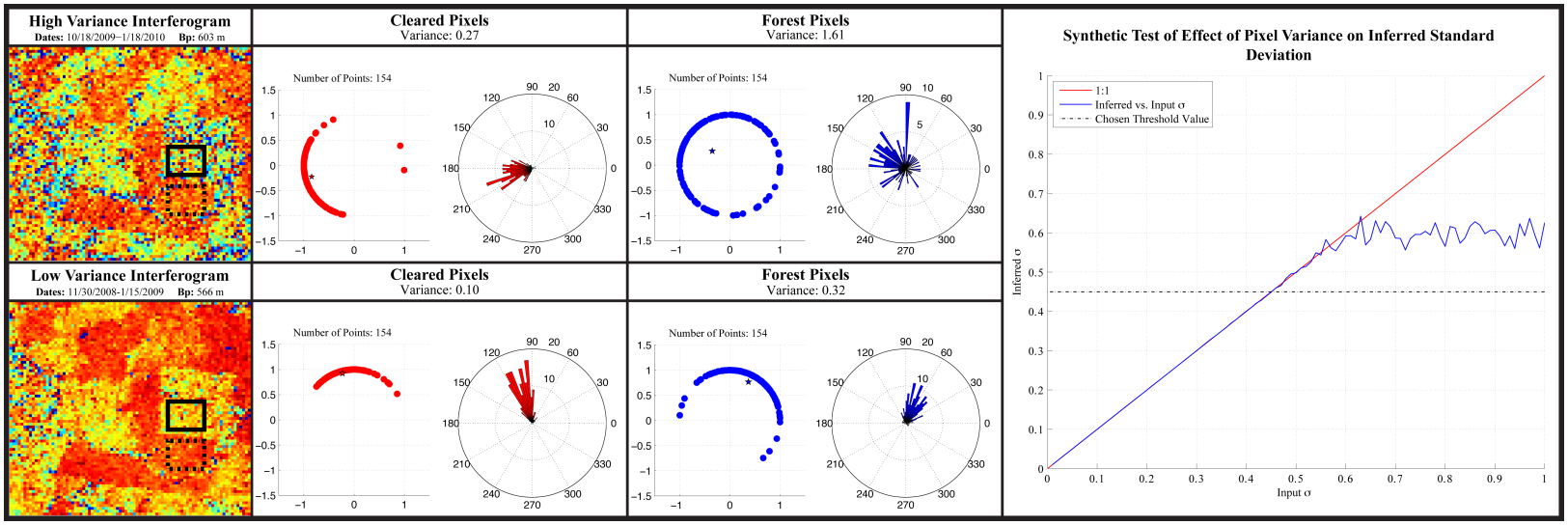

Figure 2.8: Complex phase values for an interferogram with high variance and low variance, illustrating the relative magnitudes of the average complex phase, ($\bar{\phi}$), (stars) compared with the spread of the individual phase values (small dots). Synthetic test of true variance of unwrapped, complex phase values vs. inferred variance is shown in far right panel. Note how inferred variance never extends beyond a level of ~0.6x2π.

$$z = \frac{mRsin\theta\lambda}{4\pi} \qquad \text{(Eq. 2.4)}$$

where z is the predicted canopy height; R is range between the satellite and ground; θ is the satellite look angle measured from nadir; and λ is the wavelength of the sensor. To find the canopy height that minimizes E, we perform a grid search through heights ranging from 0 to 100 meters. At each height, we compute the error, E, between the complex values of predicted and observed phase difference to avoid issues with unwrapping (Figure 2.9).

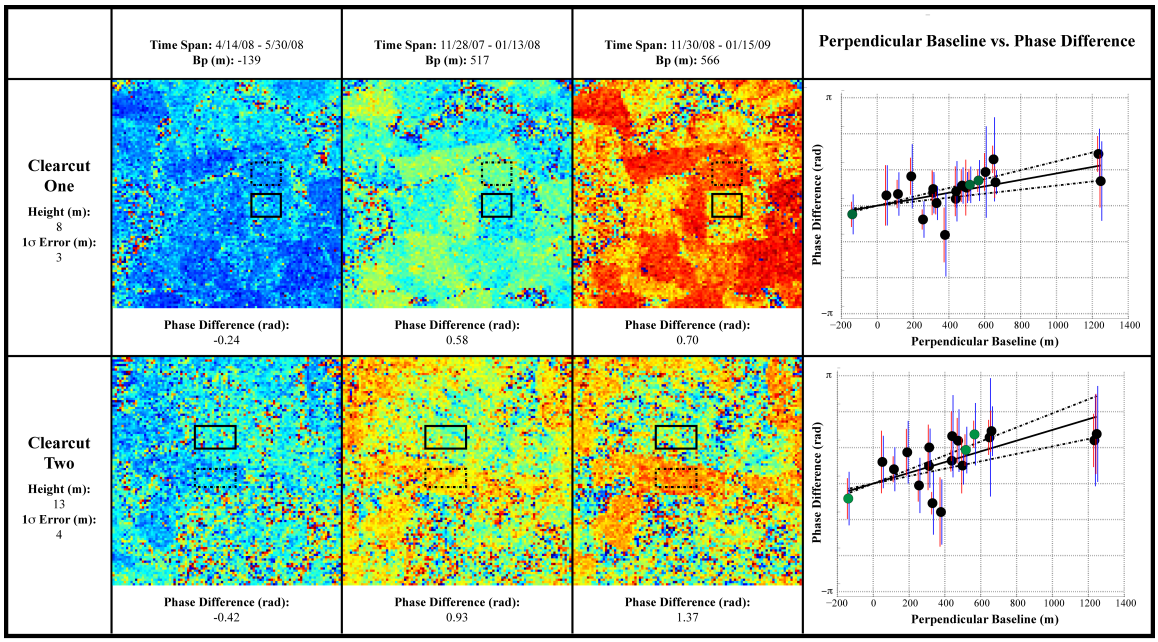

Figure 2.9: Two adjacent forested and cleared regions (locations indicated in Figure 2.3) observed in 3 interferograms. Perpendicular baseline value of interferograms increases to the right. Note that as baseline increases, so does the difference in average phase between cleared and forested pixels. Locations of cleared (within dotted box) and forested (within solid box) pixels used to calculate phase difference are indicated. In perpendicular baseline vs. phase difference plots, green dots indicate the phase differences observed in the example interferograms to the left. Black dots indicate the phase difference values for the rest of the set of interferograms. Red and blue bars indicate the 1σ values of phase for cleared and forested pixels, respectively.

2.3 Results

2.3.1 Regional Canopy Height Estimates

Our map of canopy heights determined for the Pacific Northwest using the methods discussed above contains several key features (Figure 2.10). The Olympic Peninsula, a region known for dense forests and large trees, is associated with a low density of canopy height observations. This is due to forest conservation efforts over much of the Olympic Peninsula. Without cleared areas to use as a reference for the Earth's surface beneath the forests, estimates of canopy height cannot be made using our InSAR-based method. The Tillamook and Clatsop state forests in NW Oregon are associated with similarly low densities of observations.

In general, our canopy height estimates increase towards the coast and decrease towards the eastern part of Washington and Oregon. This is largely a climatic effect, as the eastern part of Oregon and Washington is much drier than the coasts and the forests are less dense, with shorter trees. The Willamette Valley Basin, home to approximately 70% of Oregon's population and a great deal of its agricultural production, is associated with relatively low estimated canopy heights [*Loy*, 2001].

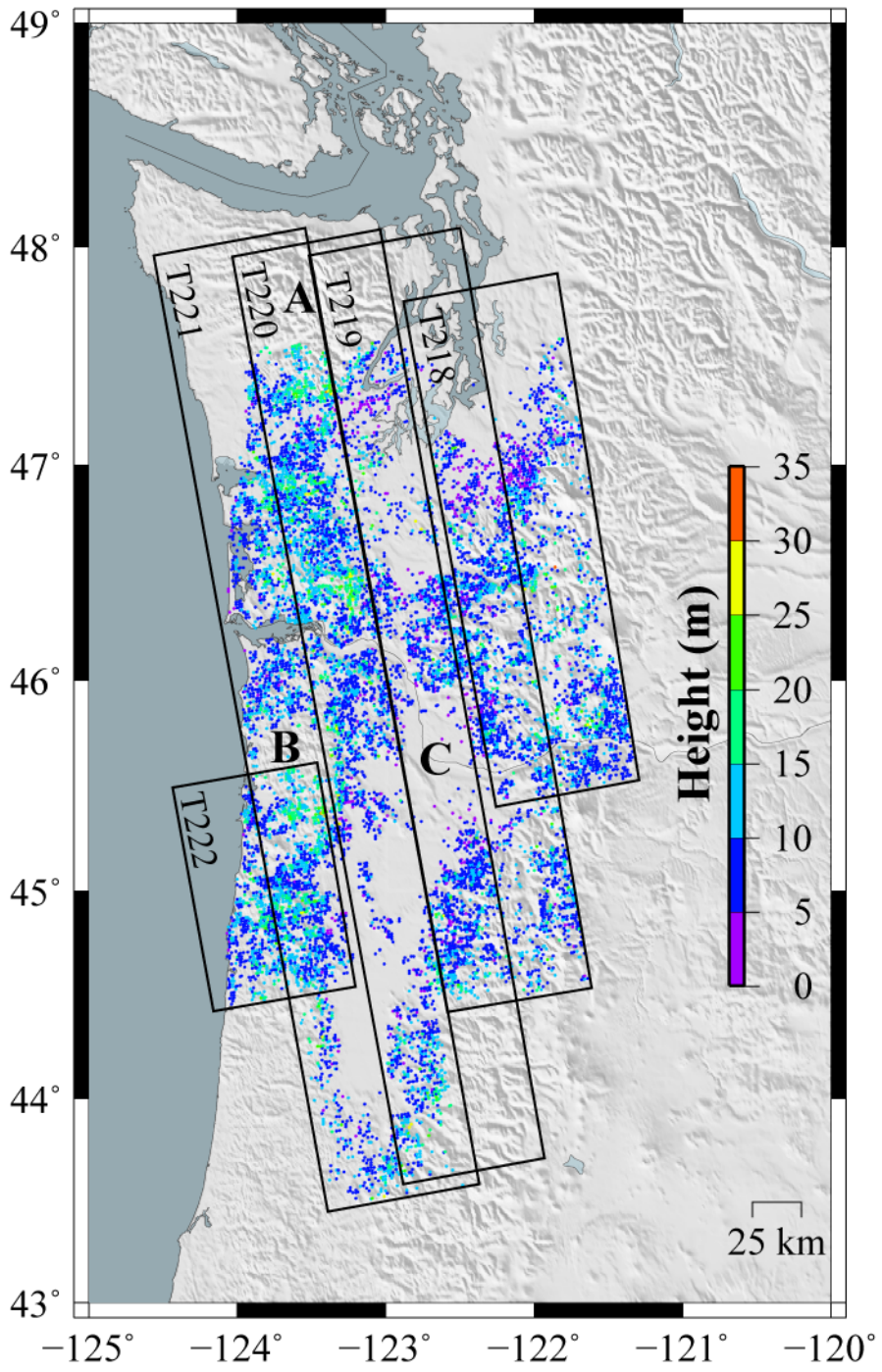

Figure 2.10: Map view of canopy height estimates determined for the Pacific Northwest. The Olympic Peninsula (a), Tillamook and Clatsop State Forests (b), and Willamette Valley Basin (c) are labeled.

2.3.2 Comparison between overlapping SAR datasets

The adjacent satellite paths used in this study overlap by ~30 km. SAR imagery covering the regions of overlap will have different acquisition dates, range values, and look angles for the same ground location, allowing us to assess the consistency of our results (Figure 2.11). Here we examine the region of overlap between paths 221 and 222, frame 890. The 1σ error bounds of the inferred heights for each frame are consistent with each other.

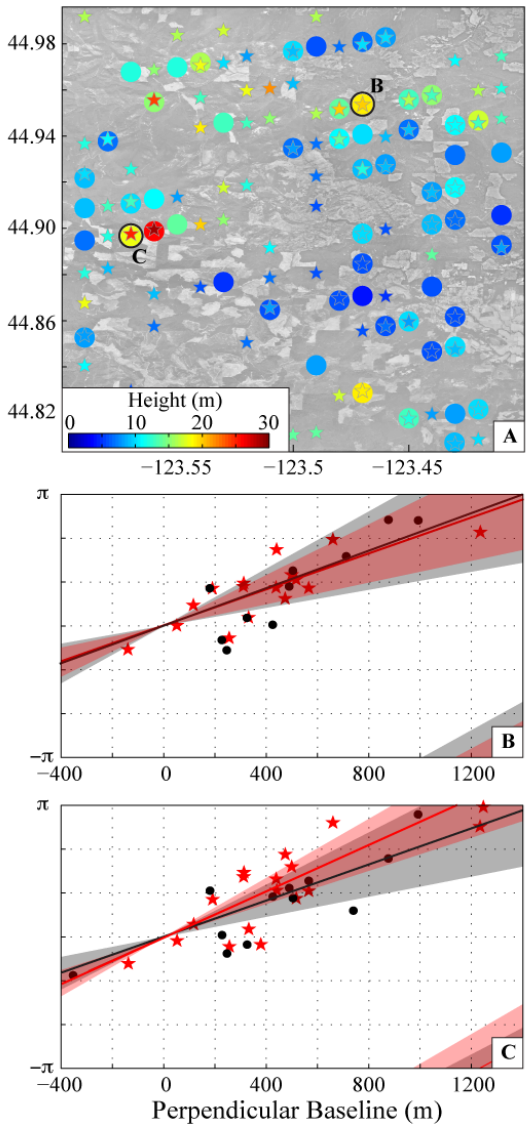

Figure 2.11: (a) Overlapping region of frame 890, tracks 221 and 222. Stars indicate canopy height measurements determined within track 222; circles indicate 221 values. Overlapping measurements labeled (b) and (c) correspond to perpendicular baseline vs. phase difference plots below. (b) Plot of phase difference vs. perpendicular baseline for well-agreeing height value and (c) disagreeing height value. Though the canopy height estimate determined for the same region in both tracks in (c) is not the same, the estimates fall within our stated error of one another.

2.3.3 Comparison with LiDAR

We compare our inferred canopy heights with LiDAR measurements. We use LiDAR data obtained by the Oregon Department of Geology and Mineral Industries (DOGAMI), available online through the NSF OpenTopography Facility, for the two cleared regions presented in Figure 2.9 (Figure 2.12). We differenced the first and ground returns for an estimate of canopy height. Transects of LiDAR data through the forests surrounding the cleared areas of interest show that the InSAR-based estimates of canopy height are approximately 50% shorter than the LiDAR-based values, a result that is consistent with the expected increased depth of interaction for L-band SAR sensors compared with LiDAR.

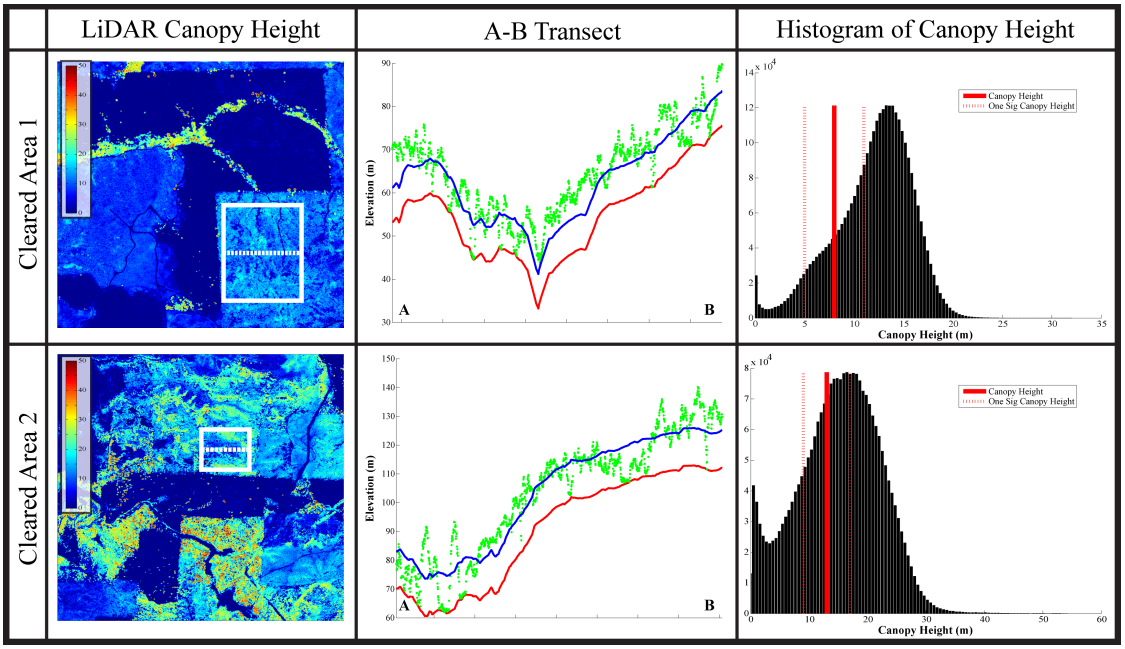

Figure 2.12: Average canopy height determined using our methods compared with LiDAR data for regions shown in Figure 2.9. First panel: map view of LiDAR-derived canopy height estimates (in meters) for forested and cleared regions. Solid white box: region of selected canopy heights for histogram. Dotted line indicates location of canopy height transect. Red line in second panel – ground location; green dots – first returns of LiDAR data; blue line – InSAR-determined canopy height. Third panel: histogram of canopy heights within solid box in first panel compared with average canopy height determined using our methods.

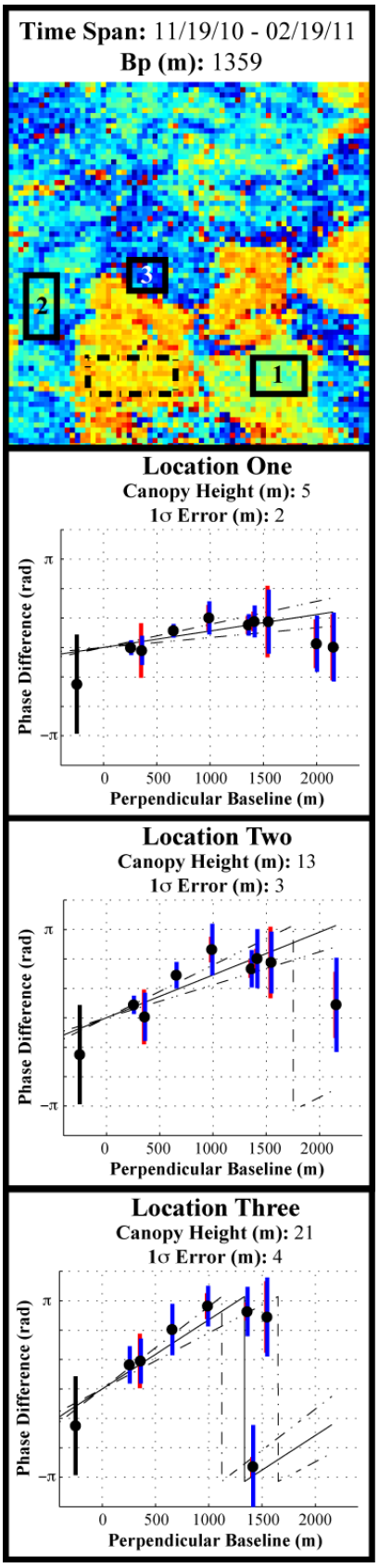

2.3.4 Multiple Stages of Clearing

Our approach estimates canopy height by comparing pixels flagged as either cleared or forested between 2006 and 2011. However, many interferograms display coherent phase differences between adjacent forested regions as well, indicative of varying canopy heights between plots of forest that have been cleared at different times in the past (Figure 2.13). Our method only extracts an average height estimate for these regions of multi-stage regrowth. Given a sufficiently long time span of SAR acquisitions, determination of changing canopy height over a number of years should be possible.

Figure 2.13: Canopy height estimates in a region where clearing has occurred multiple times. Black solid boxes indicate regions where forest is currently growing. Black dotted box outlines a cleared area. All phase difference values are taken in relation to this cleared area. Perpendicular baseline vs. phase difference plots, as well as canopy height estimates, are given for location one, two, and three. Coherent phase differences between three forested areas are indicative of varying regional canopy height due to clearing and subsequent afforestation occurring at different times.

2.3.5 A Note on SRTM vs. NED Elevation Models

DEMs derived from SRTM products are frequently used in InSAR studies to remove the effects of topography. As was found in the Kellndorfer (2004) study, the interaction of C-band radar with vegetation allows for the generation of canopy height maps. We compare the results of our approach applied to path 222, frame 890 using both the SRTM and NED DEM. In some regions, processing using the SRTM DEM results in larger phase differences and estimates of canopy height than what is observed using the NED product (Figure 2.14). We find that these locations correspond to regions where the forest was cleared after SRTM (February 2000), but before the acquisition of SAR imagery used in our analysis (Figure 2.15).

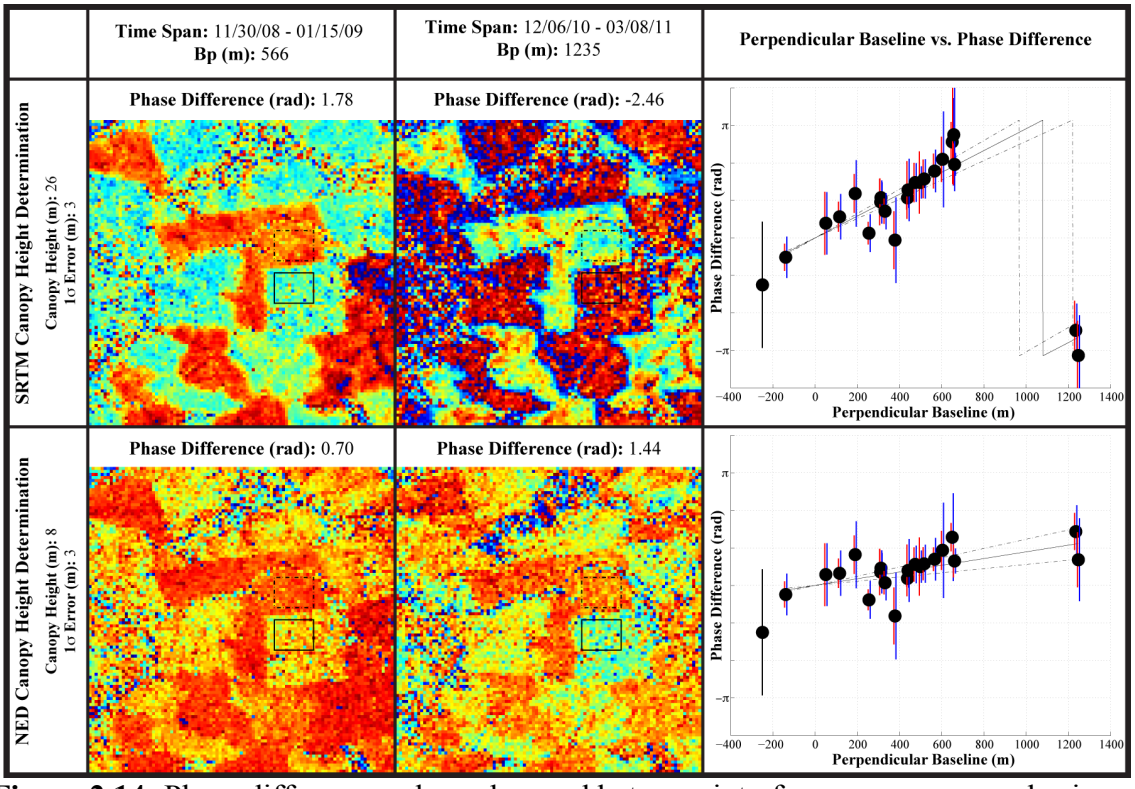

Figure 2.14: Phase difference values observed between interferograms processed using the SRTM DEM (top row) and the NED DEM (bottom row). Associated phase difference vs. baseline plots are presented in third column. Phase differences are larger in interferograms processed with the SRTM DEM, resulting in larger canopy heights.

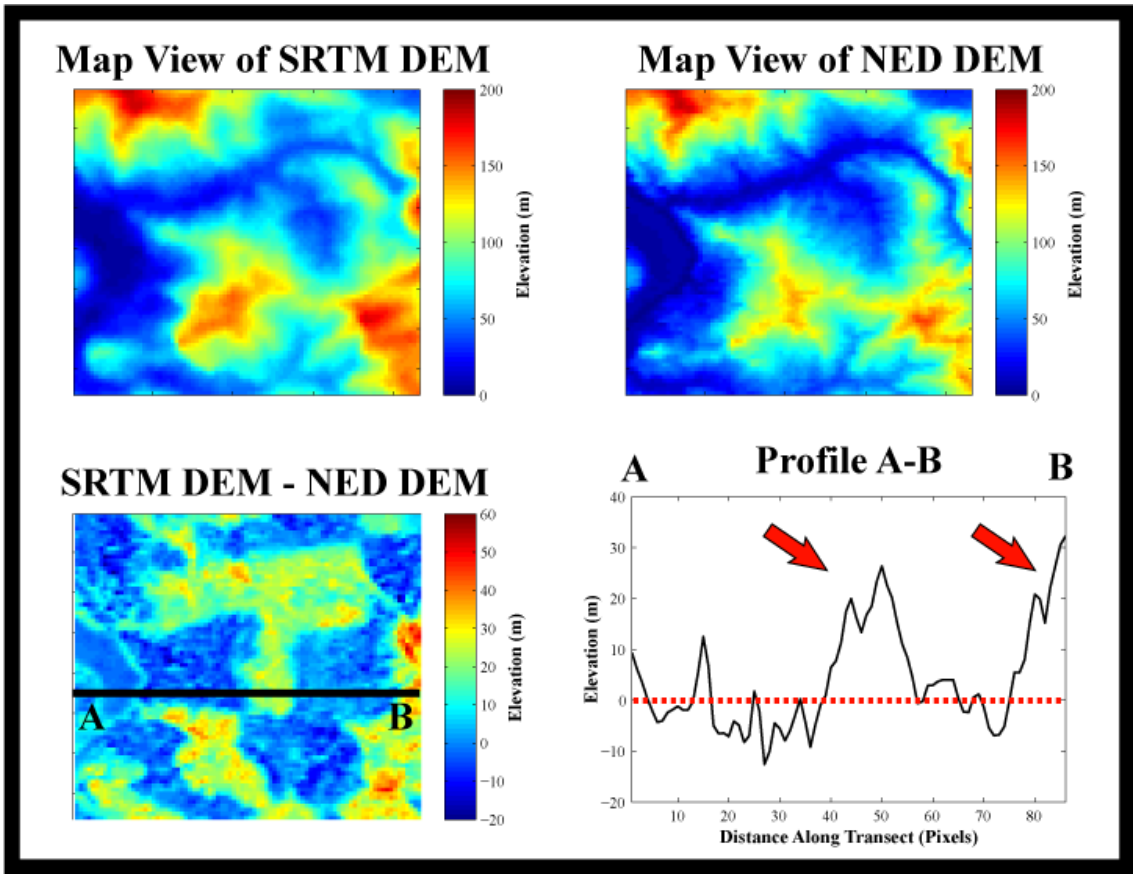

Figure 2.15: (a) Map view of the SRTM DEM and (b) the NED DEM at the same location. (c) Value of SRTM DEM – NED DEM for same region shown in (a) and (b). (d) Transect A-B along black line in (c), showing the difference in height between the two elevation products. Red arrows indicate regions that were vegetated during the SRTM survey in 2000. For the duration of the time span of the Landsat data used in this study (2006 – 2011), the T-shaped area is cleared, indicating that it was harvested sometime between 2000 and 2006.

2.4 Conclusions

Monitoring of forest stock globally and at frequent time intervals is critical to efforts to study and mitigate anthropogenic effects on climate change. We have presented a method for determining regional canopy height using phase differences between adjacent cleared and forested regions observed in L-band interferograms. Our canopy height map spans the Pacific Northwest, one of the largest temperate forests in the world

and a region of great economic and ecological interest. Our results are consistent with LiDAR data, another commonly used remote sensing method for studying vegetation structure. Our methods are restricted to regions that have undergone clearing within the past few years, providing no canopy height estimates in other regions of importance, such as protected forests.

The steadily increasing catalog of publicly available SAR imagery will allow further improvement to this and other SAR-based approaches. The use of C- or X-band data would allow better inferences of canopy height than would be possible using L-band-based proxies alone. Shorter repeat intervals such as those proposed for satellites set to launch within the next years will result in improved coherence and time series that can better identify changes in forest coverage and canopy height.

CHAPTER 3

THE CENTRALIA POWER PLANT

3.1 Introduction

Chapter 2 focused on a baseline-dependent signal caused by differences between the height of dominant scatterers within adjacent vegetated and clearcut regions. This chapter will focus on a baseline-dependent signal caused by changes in the actual elevation of the ground surface. As mentioned previously, processing of interferograms necessitates the removal of an estimate of topography so that crustal deformation signals may be examined. Inaccuracies in the DEM will lead to signals in the interferogram that may be interpreted as crustal deformation. This chapter examines one such signal associated with the Centralia Power Plant and Coal Mine in Centralia, Washington.

The Centralia Coal Plant and associated mine were first brought into production in 1971 (TransAlta Corporation website). The Calgary-based energy company TransAlta acquired the plant and mine in 2000 for $554 million from a group of 8 utilities: PacifiCorp, Avista, City of Seattle, City of Tacoma, Snohomish County Public Utility District (PUD), Puget Sound Energy Inc., Grays Harbor PUD, and Portland General Electric (TransAlta Corporation website). The coal plant has a net capacity of 1340 megawatts and is the largest baseload power source in the state, providing approximately 10% of Washington's power (TransAlta Corporation website). It is currently the only coal plant in Washington, and is in the process of being phased out by 2025 as the plant converts to natural gas as its primary power source (TransAlta Corporation website). In addition to its coal power generators, the Centralia Power Plant is supplemented by natural gas and hydroelectric sources.

The Centralia Coal Mine is a sub-bituminous surface coal mine located 10 kilometers northeast of the city of Centralia. The mine provided coal to the power plant until 2006, when operations were shut down. From the time the coal mine opened for production in 1971 until it was shut down in 2006, 1.5 billion yards of material was removed and 158 million tons of coal was mined (TransAlta Corporation website). Today, the mine and its surroundings are undergoing reclamation. Of the total 7700 acres of land that was disturbed during the productive years of the mine, 2600 have been reclaimed and restored to their natural state or converted to recreational or agricultural uses (TransAlta Corporation website).

3.2 Methods

3.2.1 Data

We use L-band (λ = 23.6 cm) PALSAR data collected by ALOS between February 20, 2007 and December 1, 2010 (Table 3.1). Interferograms were generated using the Repeat Orbit Interferometry PACkage (ROI_PAC), an open-source software package for processing SAR acquisitions, developed jointly by the Jet Propulsion Laboratory (JPL) and Caltech [*Rosen et al.*, 2004a]. We generate all possible interferograms with perpendicular baselines <2500 m and temporal baselines <~1 year. We rectify all unwrapped interferograms to a common grid in radar coordinates before further processing. Interferograms were downsampled 12 times in azimuth and 4 times in range. The power spectrum filtering method was used (filter strength of 0.2) to reduce phase noise due to temporal and geometric decorrelation [*Goldstein and Werner*, 1998]. Interferograms were unwrapped using the Statistical-Cost, Network-Flow Algorithm for

Phase Unwrapping (SNAPHU) [*Chen and Zebker*, 2002]. After unwrapping, the average phase value over two regions near the Centralia site that are not expected to have experienced any deformation during the time span of our interferogram set was removed in order to reduce the effect of long-wavelength errors due to atmospheric water vapor and errors in our knowledge of satellite positions.

Table 3.1: Interferograms used to characterize elevation changes at the Centralia power plant and mine.

Track Number	Frame Number	Date One (yymmdd)	Date Two (yymmdd)	Perpendicular Baseline (m)
219	920	070220	070523	225.1
		070523	070708	684.5
		070708	070823	97.9
		080223	080409	547.6
		080409	080525	-86.9
		100228	100415	275.5
		100415	100531	137.6
		100831	101016	305.0
		101016	101201	38.3

Interferometric processing for the purposes of non-topographic studies requires removal of the effects of topography from the interferogram, usually in the form of a digital elevation model (DEM). Differences between these two products, as well as the residual topographic signal observed in the InSAR, are related to changes in elevation of the ground surface at the Centralia site. We use the 1 arc-second National Elevation Dataset (NED) product, produced by the USGS [*Gesch et al.*, 2002; *Maune*, 2007]. The NED is a bare-earth elevation product, updated bimonthly to integrate new elevation datasets as they become available. We also use the Shuttle Radar Topography Mission (SRTM) elevation product, acquired in February 2000 [*Farr et al.*, 2007].

3.2.2 Observed topographic changes

If a digital elevation model (DEM) does not account for all of the topographic variation present in an interferogram, a baseline-dependent signal will result. Figure 3.1 shows one of the interferograms used in this study, including the signal that we attribute to changes in elevation at the Centralia Power Plant site. Both positive and negative features are prominent in this and the other interferograms.

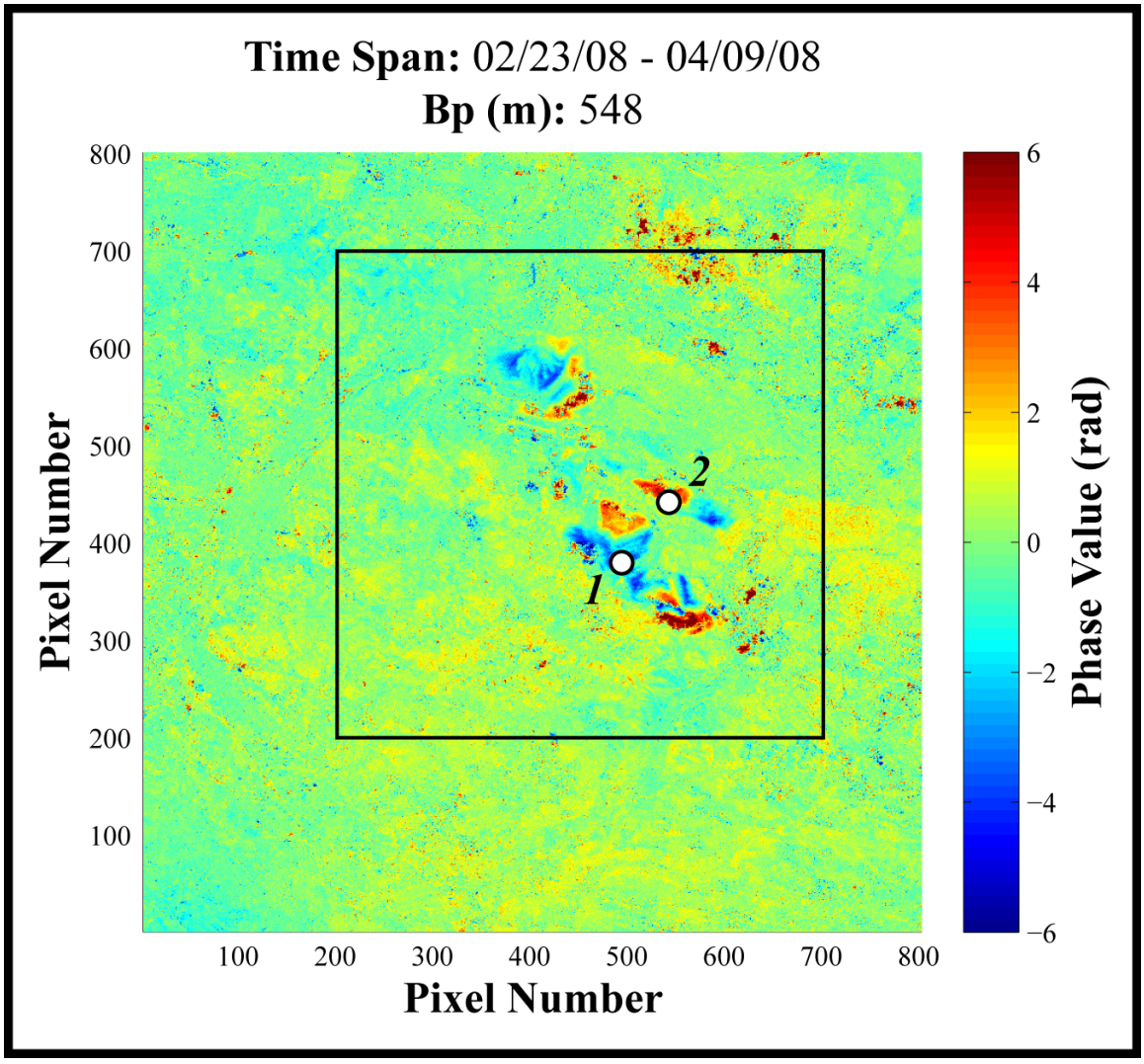

Figure 3.1: Centralia Power Plant site as seen in an unwrapped interferogram (time span February 23 – April 9, 2008; perpendicular baseline 548m). Black box outlines region of Centralia site used in figures 3.3 – 3.7. Points 1 and 2 indicate pixels shown in Figure 3.2.

The dependence of observed topographic height on interferometric phase is:

$$H = \frac{-\lambda R sin\theta}{4\pi} m \quad \text{(Eq. 3.1)}$$

where H is the topographic height; λ is the wavelength of the transmitted signal; θ is the look angle of the sensor measured from nadir; and m is the slope of the line relating perpendicular baseline (*Bp)* and phase difference between the first and second SAR acquisitions ($d\phi$) (Figure 1.1). By determining the slope of the line relating perpendicular baseline to interferometric phase on a pixel-by-pixel basis for the set of 9 interferograms, we determine the residual topographic height (H) of pixels at the Centralia Power Plant site.

3.3 Discussion

3.3.1 DEM error map using NED DEM

Figure 3.2 depicts the baseline- and time-dependence of pixels 1 and 2 shown in Figure 3.1. Both pixels show a strong correlation with perpendicular baseline and no apparent time-dependence, suggesting that the observed signal is due to changes in ground elevation since the generation of the NED DEM. Using equation 3.1, we determined the topographic height (*H)* unaccounted for by removal of the NED DEM from our interferograms at each pixel. Figure 3.3 shows a map view of the calculated DEM error observed in the region immediately surrounding the Centralia Power Plant site.

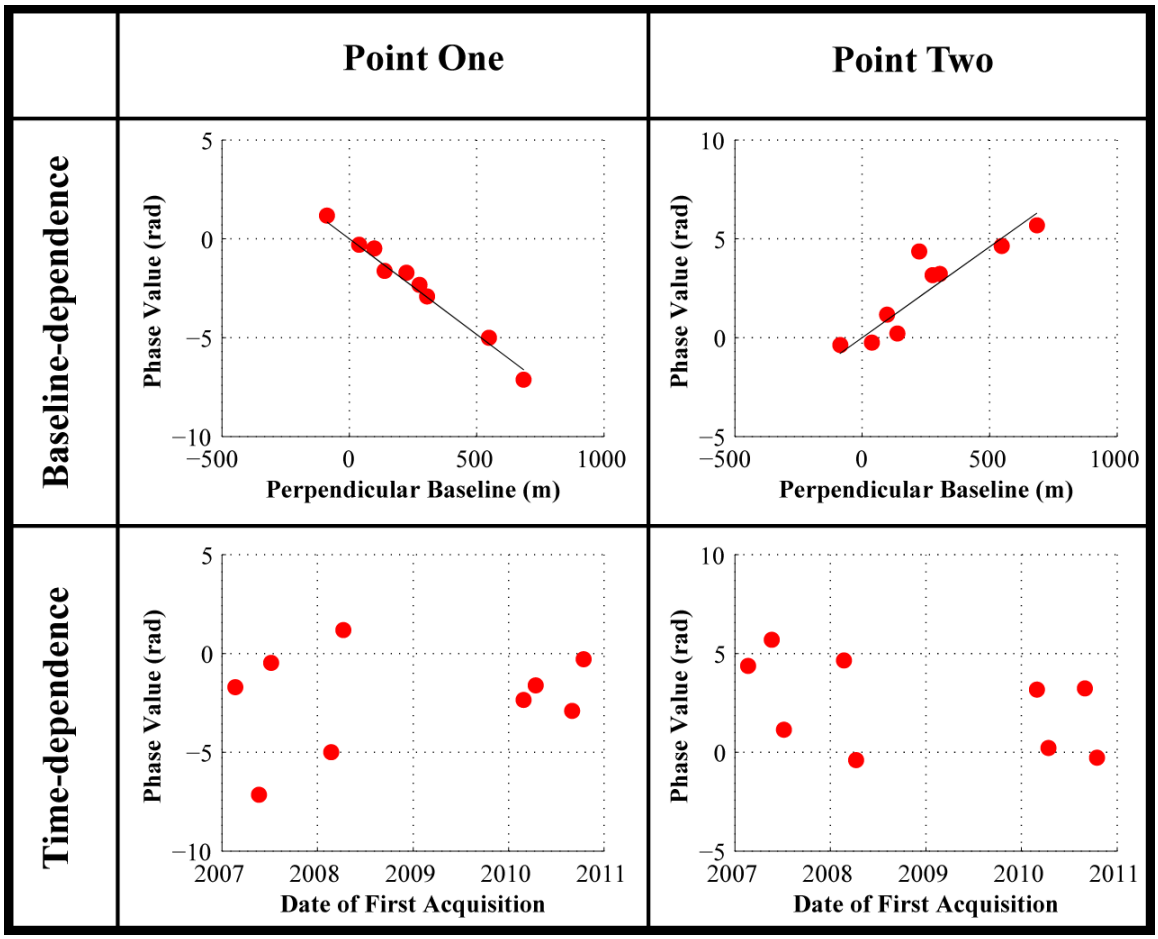

Figure 3.2: Baseline- and time-dependence of pixels within positive and negative phase change regions of Centralia site. Observed baseline-dependence is strong, while time-dependence is not.

3.3.2 SRTM vs. NED Errors

The NED DEM is compiled using a variety of sources, and it is thus difficult to determine when and from what source the topographic estimate in the region surrounding the Centralia Power Plant was derived [*Gesch et al.*, 2002; *Maune*, 2007]. In order to place more rigorous constraints on the timing of ground displacement that has caused our observed DEM error, we also compared the NED and SRTM DEMs. Since the SRTM DEM was acquired in February of 2000, any DEM errors observed by processing our interferograms with the SRTM DEM must have been caused by changes in ground

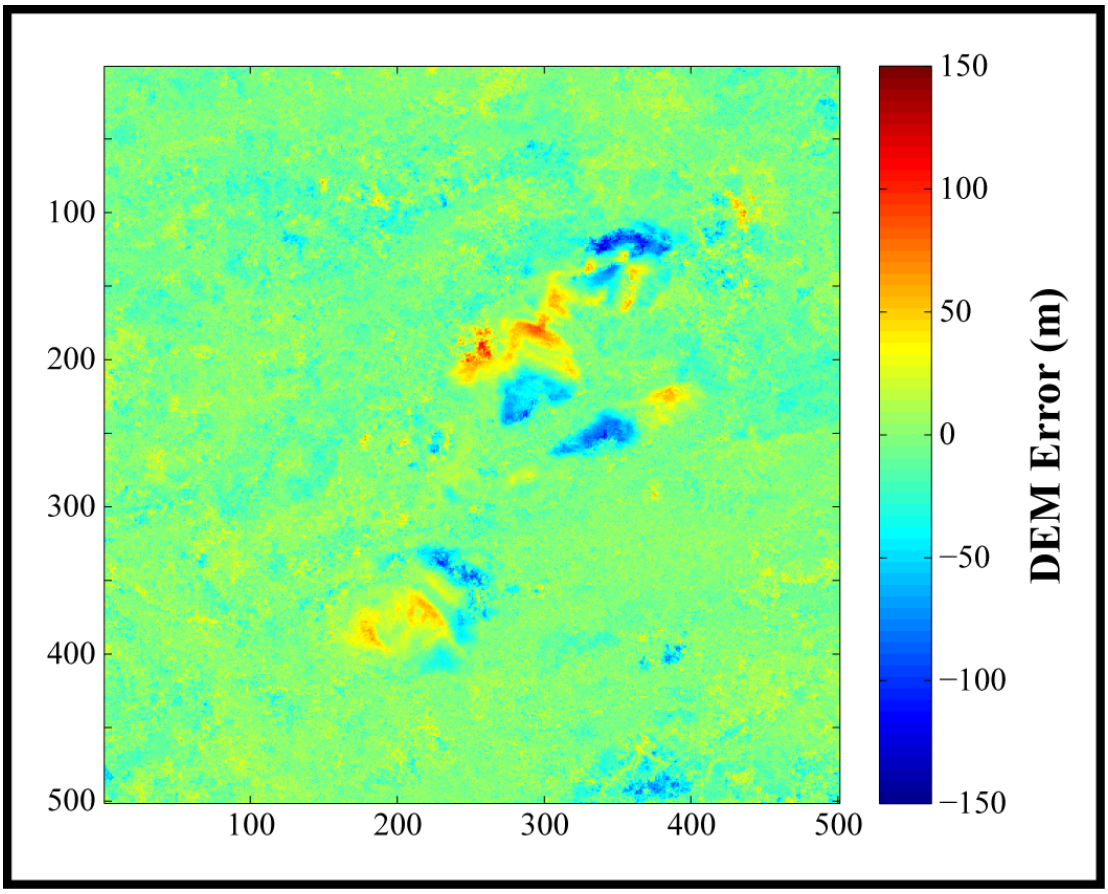

Figure 3.3: Map view of calculated DEM error at the Centralia Power Plant site.

elevation after this date. By differencing the SRTM and NED DEMs, we obtain an estimate of how much elevation change occurred between the time of generation of the NED DEM and February 2000 (Figure 3.4).

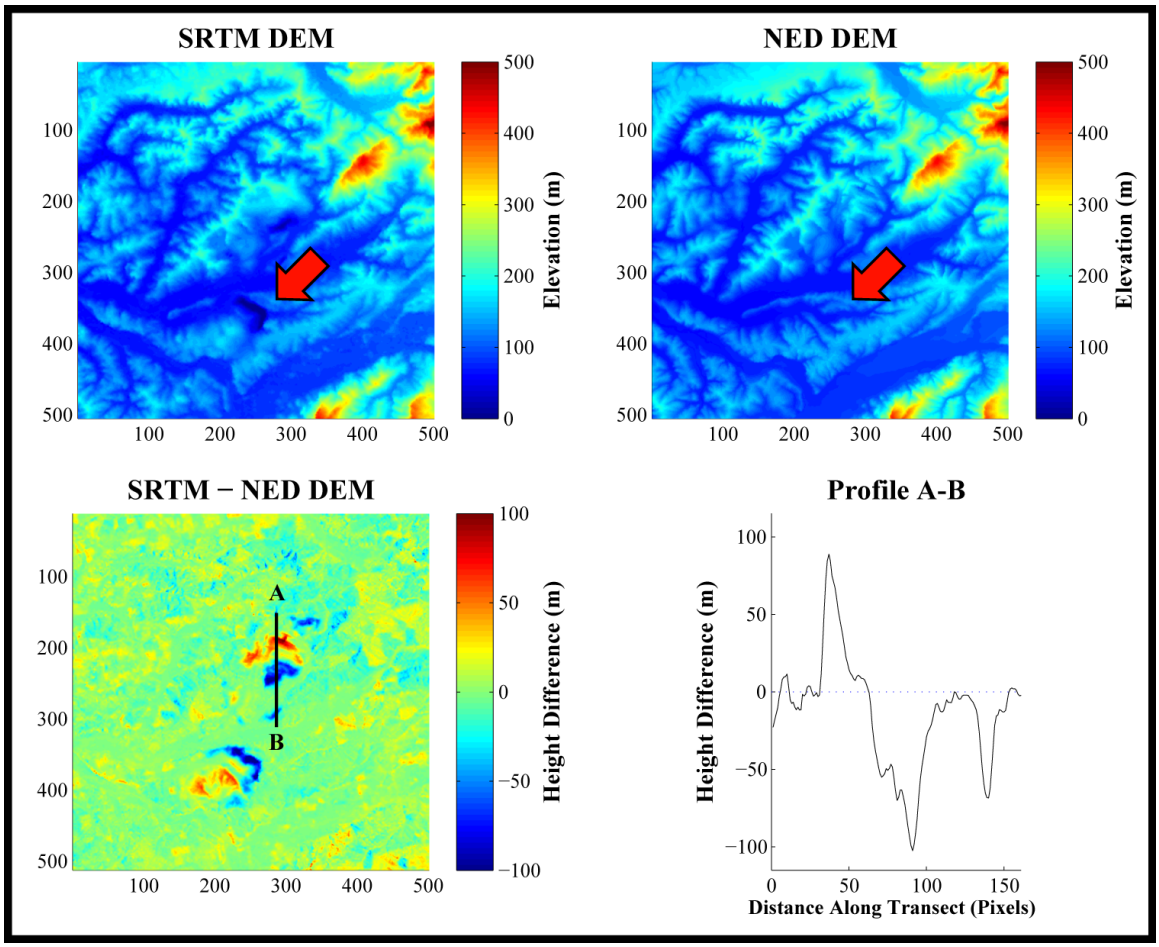

Figure 3.4: Comparison of (a) SRTM and (b) NED DEMs in the region of the Centralia Power Plant site. Red arrow points to a depression associated with the Centralia coal mine that is observed in the SRTM DEM but not in the NED DEM. (c) The difference between the SRTM and NED DEMs. (d) Transect marked A-B in (c) illustrating the large elevation change between the SRTM and NED DEMs.

The difference between the SRTM and NED DEMs (Figure 3.4) does not entirely account for the signal present in the InSAR data (Figure 3.5). The remaining signal must, therefore, be due to activities that occurred after February 2000.

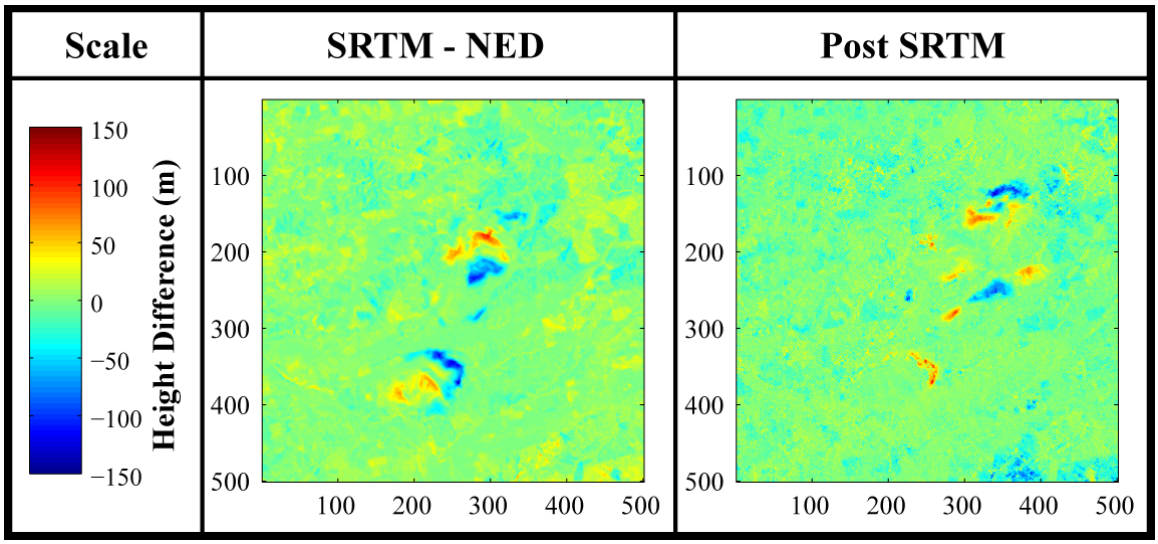

Figure 3.5: Effect of removing difference between SRTM and NED DEMs from DEM error observed in our interferograms. (a) Difference between SRTM and NED DEMs in the region of the Centralia site. (b) Error remaining in interferograms after removal of (a) from elevation change observed in interferogram set.

3.3.3 Time-dependency of signal within time span of interferograms (2007-2010)

The temporal resolution of this study is limited by the distribution of SAR data acquired after the generation of the SRTM DEM in 2000. ALOS imagery was only acquired from 2007-2010, so we are not able to resolve any changes in ground elevation that occurred between 2000 and 2007. To characterize post-2007 variability, we divided the interferograms into two sets: those predating 2009 and those acquired after 2009. We performed the same calculation of height difference used to generate the full elevation change map (see Figure 3.3) for each set individually (Figure 3.6). The similarity between the pre- and post-2009 elevation change maps suggests that the majority of the ground displacement occurred before the time span of our interferogram set. Differencing the pre- and post-2009 elevation change maps shows that no significant land change has occurred since 2007 (Figure 3.6).

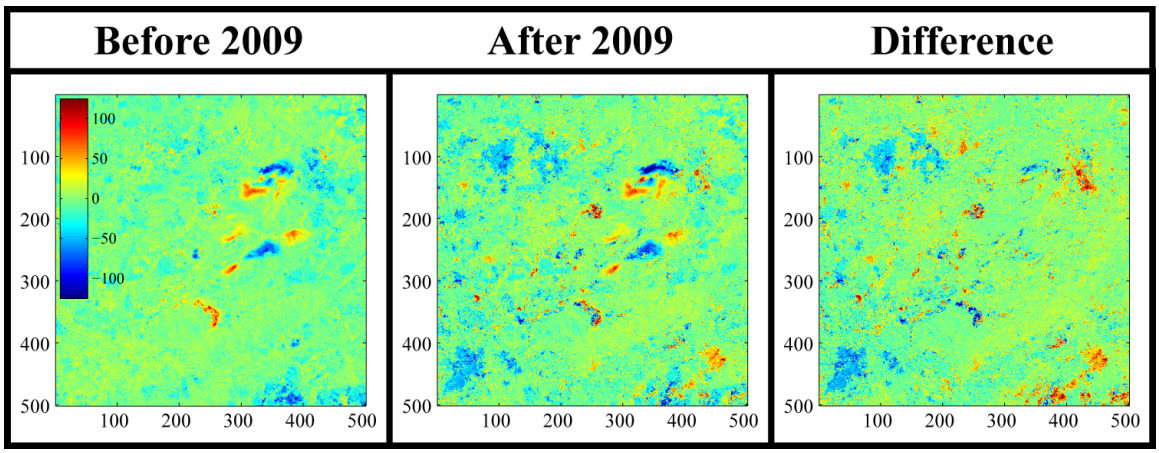

Figure 3.6: DEM errors observed in InSAR data acquired before 2009 and after 2009. Far right panel is difference between first and second panels.

3.3.4 Volumetric Displacement

We estimate the volume of material moved by multiplying the area of pixels within the regions of observed elevation changes (Figure 3.7) by the calculated elevation changes at the Centralia Power Plant site. The pixel sizes are 42.3 m in azimuth and 18.7 m in range. The volumes of material displaced for each feature in Figure 3.7 are given in Table 3.2. The volume of material removed from the site based on our calculations is 2.2×10^8 m^3, approximately 5 times less than what has been reported as mined at the site (1.5 billion yards, or 1.15×10^9 m^3) since 1971. The discrepancy between our estimates and the total amount of material moved is likely due to the generation date of the NED DEM. Though the date of acquisition is unknown, there is a strong possibility it represents land changes occurring after 1971, and thus does not account for the total amount of material mined.

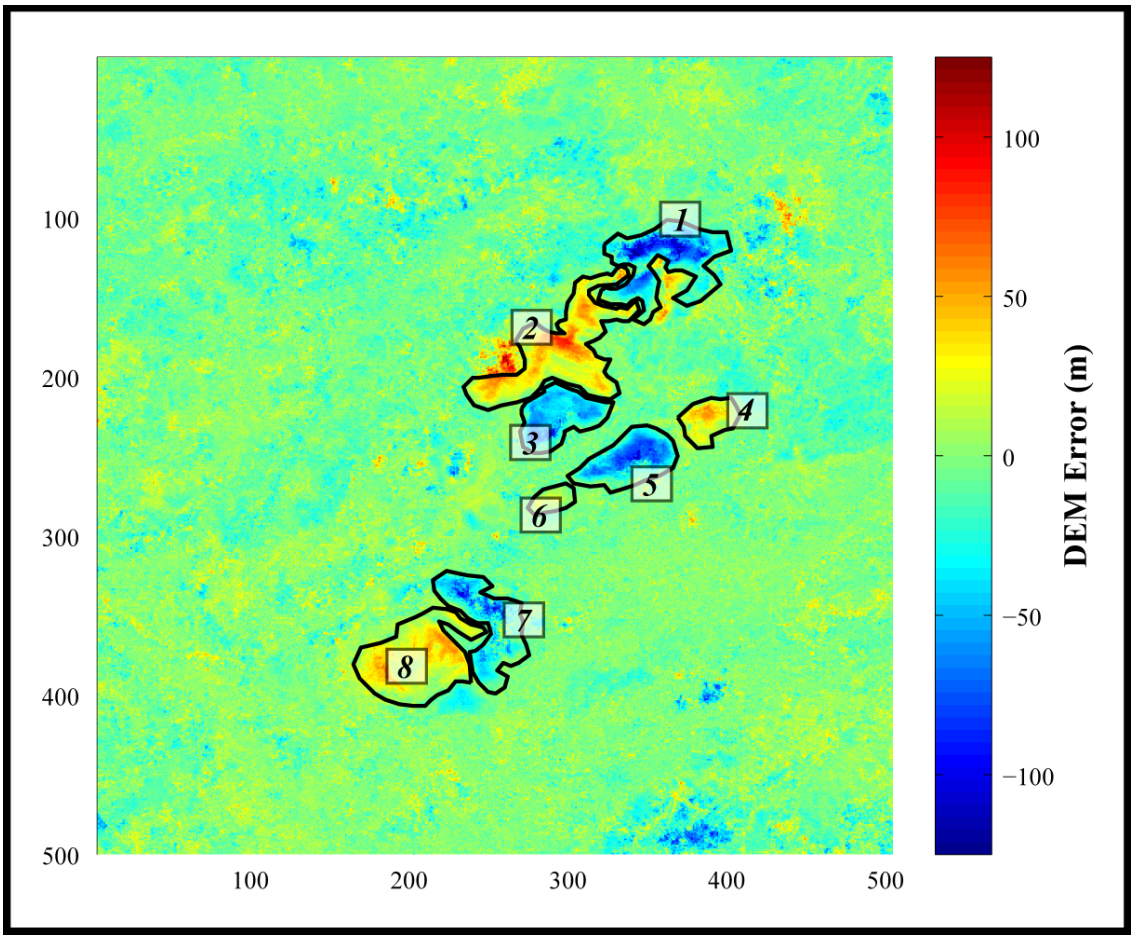

Figure 3.7: Eight regions of calculated volume change are outlined in black and numbered. The volume of displaced material for each area is given in Table 3.2.

Table 3.2: Calculated volume change using interferogram set processed with NED DEM (Height Difference); volume difference between NED and SRTM DEMs (SRTM-NED); and volume change after SRTM acquisition (Post SRTM) for each of the 8 regions indicated in Figure 3.7.

Region No.	**1**	**2**	**3**	**4**	**5**	**6**	**7**	**8**	**Total**
No. Pixels	2642	3581	1524	794	1678	383	2088	3031	
Height Difference (10^7 m^3)	-8.0	7.5	-4.6	1.4	-5.2	0.19	-4.7	5.1	-8.31
SRTM-NED (10^7 m^3)	-3.3	5.2	-6.1	-0.53	-0.75	-0.83	-7.4	5.4	-8.35
Post SRTM (10^7 m^3)	-4.7	2.3	1.5	1.9	-4.4	1.0	2.8	-0.32	0.04

3.4 Conclusion

In this chapter, we have examined a baseline-dependent signal associated with a power plant and coal mine located in Centralia, Washington. The signal is attributed to changes in ground surface elevation associated with movement of ground due to operations at the power plant and mine. The magnitude of the observed elevation change has been calculated for all pixels near the site, and constraints on timing of ground displacement have been determined. The total volume of material moved has been calculated for regions with the largest observed elevation changes.

The implications of this work for InSAR studies of crustal deformation are broad. InSAR studies of subtle ground deformation signals require high-quality DEMs, particularly in cases where too few interferograms exist to allow robust identification of the baseline-dependent component of a signal. By improving DEMs used for processing, we can avoid spurious analyses of signals misidentified as crustal deformation that may instead be attributable to DEM error. Deconvolving baseline- and time-dependent signals in interferograms can be challenging, but it is a necessary process for correct interpretation of crustal deformation signals. Our study shows that, even within a relatively short period of time in the early 2000's, anthropogenic activities can profoundly affect topography. Since regions where mining and extraction or injection of subsurface fluids may be associated with other signals of interest, such as triggered seismicity and landslides, separating out the temporal- and baseline-dependent components of the observed interferometric time series is critical.

APPENDIX A

Interferogram Set for Determination of Canopy Height

Track Number	Frame Number	Date One (yymmdd)	Date Two (yymmdd)	Perpendicular Baseline (m)	No. Ints.
218	910	070621	070806	310.4	21
		070806	070921	-30.0	
		070921	071106	712.3	
		071106	071222	-93.6	
		071222	080206	862.8	
		080206	080323	236.7	
		080323	080508	603.3	
		080808	080923	929.5	
		080923	081108	226.4	
		081108	090208	929.8	
		090208	090626	928.2	
		090626	090811	-88.9	
		090811	090926	563.9	
		090926	091227	667.1	
		091227	100211	640.4	
		100211	100329	332.7	
		100329	100514	147.4	
		100514	100629	162.5	
		100629	100929	819.1	
		100929	101114	-422.1	
		101114	110214	1534.7	
218	930	070621	070806	309.6	25
		070806	070921	-18.9	
		070806	071106	693.7	
		070921	071106	712.6	
		071106	080206	786.4	
		080206	080323	253.6	
		080323	080508	603.1	
		080808	080923	928.7	
		080923	081108	231.7	
		080923	090208	1176.4	
		081108	090208	945.1	
		090208	090626	943.2	
		090626	090811	-80.9	
		090811	100211	1893.8	
		100211	100329	345.1	
		100211	100629	659.6	
		100329	100514	151.9	

		100329	100629	314.5	
		100514	100629	162.6	
		100514	100929	990.8	
		100514	101114	586.7	
		100629	100929	828.1	
		100929	101114	-404.2	
		100929	110214	1135.1	
		101114	110214	1539.0	
219	890	070105	070220	1866.6	28
		070220	070523	191.6	
		070220	070708	889.1	
		070523	070708	697.6	
		070523	070823	791.8	
		070523	091013	80.0	
		070708	070823	94.4	
		070823	071123	648.0	
		071123	080108	257.3	
		080108	080223	805.8	
		080223	080409	535.1	
		080223	080525	434.2	
		080409	080525	-100.9	
		081010	090225	1184.3	
		091013	100113	527.1	
		091013	100228	1237.8	
		100113	100228	710.6	
		100113	100415	965.9	
		100113	100531	1100.7	
		100228	100415	255.4	
		100228	100831	953.5	
		100228	101016	1247.0	
		100415	100531	134.8	
		100415	100831	697.8	
		100531	100831	563.0	
		100831	101016	293.6	
		101016	101201	20.3	
		101201	110303	1167.2	
219	910	070105	070220	1856.2	26
		070220	070523	210.0	
		070523	070708	691.3	
		070523	070823	787.8	
		070708	070823	96.5	
		070823	071123	661.4	
		071123	080108	266.7	
		080108	080223	816.5	
		080223	080409	542.8	

		080409	080525	-93.6	
		081010	090225	1209.9	
		090225	091013	1582.7	
		091013	100113	542.5	
		091013	100228	1261.4	
		100113	100228	718.9	
		100113	100415	985.1	
		100228	100415	266.3	
		100228	100531	403.0	
		100415	100531	136.6	
		100415	100831	705.8	
		100531	100831	569.2	
		100531	101016	869.0	
		100831	101016	299.8	
		101016	101201	29.8	
		101016	110303	1213.4	
		101201	110303	1183.6	
220	890	070122	070309	1723.3	28
		070309	070609	157.6	
		070309	070725	430.6	
		070309	070909	734.5	
		070609	070725	273.0	
		070725	070909	303.9	
		070725	071025	787.3	
		070909	071025	483.4	
		070909	071210	647.8	
		070909	080125	1168.1	
		071025	071210	164.5	
		071025	080125	684.7	
		071210	080125	520.3	
		080125	080426	1424.1	
		090614	090730	-122.4	
		090614	090914	409.5	
		090730	090914	532.0	
		090914	091215	739.6	
		091215	100317	1185.1	
		100317	100502	230.9	
		100317	100802	575.0	
		100502	100802	344.0	
		100802	100917	35.0	
		100802	101102	268.2	
		100917	101102	233.3	
		100917	110202	1296.8	
		101102	101218	450.0	
		101218	110202	613.7	

220	910	070122	070309	1715.9	18
		070309	070609	169.5	
		070609	070725	272.6	
		070725	070909	305.5	
		070909	071025	490.7	
		071025	071210	171.8	
		071210	080125	531.1	
		080125	080426	1433.9	
		090614	090730	-117.8	
		090730	090914	537.0	
		090914	091215	747.9	
		091215	100317	1204.7	
		100317	100502	237.8	
		100502	100802	346.7	
		100802	100917	44.8	
		100917	101102	240.0	
		101102	101218	454.1	
		101218	110202	622.3	
220	930	070122	070309	1706.7	19
		070309	070609	181.7	
		070609	070725	271.8	
		070609	070909	579.0	
		070725	070909	307.5	
		070909	071210	677.0	
		071210	080125	541.5	
		080125	080426	1442.0	
		090614	090730	-113.1	
		100317	100502	244.8	
		100317	100802	593.8	
		100502	100802	349.0	
		100502	100917	403.6	
		100802	100917	54.7	
		100802	101102	301.4	
		100917	101102	246.7	
		100917	101218	704.9	
		101102	101218	458.2	
		101218	110202	630.3	
221	870	070326	070926	471.8	23
		070326	080628	-619.2	
		070926	071111	876.3	
		070926	080628	-1090.8	
		071111	071227	-308.1	
		071227	080328	1210.7	
		080628	090701	-351.5	
		090701	091001	554.1	

		091001	100101	727.7	
		091001	100216	1272.9	
		091001	100519	1763.8	
		100101	100216	545.2	
		100101	100519	1036.0	
		100216	100519	491.0	
		100216	100704	739.5	
		100216	100819	914.3	
		100216	101119	1222.9	
		100519	100704	248.5	
		100519	100819	423.4	
		100519	101119	731.9	
		100704	100819	174.9	
		100819	101119	308.5	
		101119	110219	1318.4	
221	890	070326	070926	488.8	22
		070326	071111	1365.4	
		070926	071111	876.5	
		071111	071227	-291.5	
		071111	080211	712.2	
		071111	080328	938.4	
		071227	080211	1003.7	
		080211	080328	226.4	
		080628	090701	-355.6	
		080813	080928	992.8	
		080928	081229	550.8	
		081229	090213	815.3	
		090213	090701	620.8	
		090701	091001	565.2	
		091001	100101	739.4	
		100101	100519	1062.6	
		100519	100704	246.1	
		100519	100819	425.4	
		100704	100819	179.3	
		100704	101119	504.4	
		100819	101119	325.0	
		101119	110219	1332.0	
221	910	070326	070926	505.8	18
		070926	071111	876.7	
		071111	071227	-274.8	
		071111	080328	974.5	
		071227	080211	1008.9	
		080211	080328	240.7	
		080813	080928	991.1	
		080928	081229	567.2	

		081229	090213	822.7	
		090213	090701	634.6	
		090701	091001	576.4	
		091001	100101	751.4	
		100101	100519	1089.4	
		100519	100704	243.7	
		100519	100819	427.6	
		100704	100819	183.8	
		100819	101119	341.6	
		101119	110219	1345.8	
222	890	070713	070828	312.1	20
		070828	071013	498.8	
		071013	071128	115.9	
		071128	080113	516.9	
		080113	080228	660.1	
		080228	080414	438.3	
		080414	080530	-139.3	
		080830	081130	1247.6	
		081130	090115	565.7	
		090115	090302	331.2	
		090718	090902	473.6	
		090902	091018	378.0	
		091018	100118	603.2	
		100118	100305	649.2	
		100305	100420	255.7	
		100420	100605	190.0	
		100605	100721	50.9	
		100721	100905	311.1	
		100905	101206	440.2	
		101206	110308	1234.6	

APPENDIX B

Landsat Data for Identification of Cleared Areas

Path Number	Row Number	Acquisition Date (yyyy-mm-dd)	Cloud Cover (%)
45	29	2006-08-26	0.00
		2007-08-13	0.00
		2008-08-15	0.00
		2009-07-01	0.00
		2010-08-05	2.00
		2011-07-23	0.00
45	30	2006-07-25	0.00
		2007-08-13	0.00
		2008-08-15	0.00
		2009-07-01	0.00
		2010-09-06	0.00
		2011-07-23	0.00
46	26	2006-10-04	0.00
		2007-06-01	0.00
		2008-09-23	10.00
		2009-09-10	10.00
		2010-01-16	7.00
		2011-10-18	0.00
46	27	2006-09-02	0.00
		2007-06-01	0.00
		2008-09-07	7.00
		2009-05-21	0.00
		2010-08-12	10.00
		2011-10-18	0.00
46	28	2006-07-16	0.00
		2007-03-29	0.00
		2008-09-07	0.00
		2009-05-21	0.00
		2010-08-12	5.00
		2011-10-18	0.00
46	29	2006-07-16	0.00
		2007-03-29	0.00
		2008-09-07	0.00
		2009-07-24	0.00
		2010-08-12	4.00
		2011-10-18	0.00
46	30	2006-07-16	0.00
		2007-06-17	4.00
		2008-06-19	0.00

		2009-07-24	0.00
		2010-08-12	9.00
		2011-10-18	0.00
46	31	2006-10-20	0.00
		2007-09-05	0.00
		2008-10-25	0.00
		2009-06-22	0.00
		2010-09-29	3.00
		2011-10-18	0.00
47	26	2006-10-11	0.00
		2007-07-10	0.00
		2008-09-14	0.00
		2009-05-28	0.00
		2010-10-06	0.00
		2011-09-07	0.00
47	27	2006-07-23	0.00
		2007-07-10	0.00
		2008-07-12	0.00
		2009-05-28	0.00
		2010-10-06	0.00
		2011-07-05	1.00
47	28	2006-07-07	0.00
		2007-07-10	0.00
		2008-09-14	0.00
		2009-05-28	0.00
		2010-10-06	1.00
		2011-07-05	5.00
47	29	2006-10-11	0.00
		2007-07-10	0.00
		2008-07-12	0.00
		2009-05-28	0.00
		2010-10-06	0.00
		2011-07-05	0.00
48	26	2006-06-28	3.00
		2007-05-14	1.00
		2008-08-04	6.00
		2009-06-04	0.00
		2010-07-25	0.00
		2011-04-23	0.00
48	27	2006-06-28	0.00
		2007-09-19	0.00
		2008 Date Unavailable	
		2009-06-04	0.00
		2010-10-13	0.00
		2011-04-23	2.00

BIBLIOGRAPHY

Agram, P. S., R. Jolivet, B. Riel, Y. N. Lin, M. Simons, E. Hetland, M.-P. Doin, and C. Lasserre (2013), New Radar Interferometric Time Series Analysis Toolbox Released, *Eos Trans. Am. Geophys. Union*, *94*(7), 69–70, doi:10.1002/2013EO070001.

Alaback, P. B. (1991), Comparative ecology of temperate rainforests of the Americas along analogous climatic gradients, *Rev. Chil. Hist. Nat.*, *64*, 399–412.

Amelung, F., D. L. Galloway, J. W. Bell, H. A. Zebker, and R. J. Laczniak (1999), Sensing the ups and downs of Las Vegas: InSAR reveals structural control of land subsidence and aquifer-system deformation, *Geology*, *27*(6), 483–486, doi:10.1130/0091-7613(1999)027<0483:STUADO>2.3.CO;2.

Andersen, H.-E., R. J. McGaughey, W. W. Carson, S. E. Reutebuch, B. Mercer, and J. Allan (2004), A comparison of forest canopy models derived from LIDAR and INSAR data in a Pacific Northwest conifer forest, *Int. Arch. Photogramm. Remote Sens.*, *34*(Part 3/W13), 211–217.

Andersen, H.-E., R. McGaughey, and S. Reutebuch (2008), Assessing the influence of flight parameters, interferometric processing, slope and canopy density on the accuracy of X-band IFSAR-derived forest canopy height models, *Int. J. Remote Sens.*, *29*(5), 1495–1510, doi:10.1080/01431160701736430.

Askne, J. I. H., P. B. G. Dammert, L. M. H. Ulander, and G. Smith (1997), C-Band Repeat-Pass Interferometric SAR Observations of the Forest, *IEEE Trans. Geosci. Remote Sens.*, *35*(1), 25–35.

Asner, G. P., D. E. Knapp, E. N. Broadbent, P. J. C. Oliveira, M. Keller, and J. N. Silva (2005), Selective Logging in the Brazilian Amazon, *Science*, *310*, 480–482, doi:10.1126/science.1118051.

Baltsavias, E. P. (1999), Airborne laser scanning: basic relations and formulas, *Isprs J. Photogramm. Remote Sens.*, *54*, 199–214.

Balzter, H. (2001), Forest mapping and monitoring with interferometric synthetic aperture radar (InSAR), *Prog. Phys. Geogr.*, *25*(2), 159–177, doi:10.1177/030913330102500201.

Balzter, H., A. Luckman, Skinner, C. Rowland, and T. Dawson (2007), Observations of forest stand top height and mean height from interferometric SAR and LiDAR over a conifer plantation at Thetford Forest, UK, *Int. J. Remote Sens.*, *28*(6), 1173–1197, doi:10.1080/01431160600904998.

Berardino, P., G. Fornaro, R. Lanari, and E. Sansosti (2002), A New Algorithm for Surface Deformation Monitoring Based on Small Baseline Differential SAR Interferograms, *IEEE Trans. Geosci. Remote Sens.*, *40*(11), 2375–2383, doi:10.1109/TGRS.2002.803792.

Bombrun, L., M. Gay, E. Trouve, G. Vasile, and J. Mars (2009), DEM Error Retrieval by Analyzing Time Series of Differential Interferograms, *IEEE Geosci. Remote Sens. Lett.*, *6*(4), 830–834, doi:10.1109/LGRS.2009.2026434.

Breidenbach, J., B. Koch, G. Kandler, and A. Kleusberg (2008), Quantifying the influence of slope, aspect, crown shape and stem density on the estimation of tree height at plot level using lidar and InSAR data, *Int. J. Remote Sens.*, *29*(5), 1511–1536, doi:10.1080/01431160701736364.

Bürgmann, R., P. A. Rosen, and E. J. Fielding (2000), Synthetic Aperture Radar Interferometry to Measure Earth's Surface Topography and Its Deformation, *Annu. Rev. Earth Planet. Sci.*, *28*(1), 169–209, doi:10.1146/annurev.earth.28.1.169.

Chen, C. W., and H. A. Zebker (2002), Phase unwrapping for large SAR interferograms: statistical segmentation and generalized network models, *IEEE Trans. Geosci. Remote Sens.*, *40*(8), 1709–1719, doi:10.1109/TGRS.2002.802453.

Cloude, S. R., and K. P. Papathanassiou (1998), Polarimetric SAR interferometry, *IEEE Trans. Geosci. Remote Sens.*, *36*(5), 1551–1565, doi:10.1109/36.718859.

DellaSala, D. A. (Ed.) (2011), *Temperate and Boreal Rainforests of the World: Ecology and Conservation*, Island Press, Washington, DC. [online] Available from: http://site.ebrary.com/id/10430948 (Accessed 18 June 2013).

Dobson, M. et al. (1995), Estimation of Forest Biophysical Characteristics in Northern Micigan with SIR-C/X-SAR, *IEEE Trans. Geosci. Remote Sens.*, *33*(4), 877 – 895.

Dobson, M. C., F. Ulaby, T. LeToan, A. Beaudoin, E. S. Kasischke, and N. Christensen (1992), Dependence of Radar Backscatter on Coniferous Forest Biomass, *IEEE Trans. Geosci. Remote Sens.*, *30*(2), 412–415.

Ebmeier, S. K., J. Biggs, T. A. Mather, J. R. Elliott, G. Wadge, and F. Amelung (2012), Measuring large topographic change with InSAR: Lava thicknesses, extrusion rate and subsidence rate at Santiaguito volcano, Guatemala, *Earth Planet. Sci. Lett.*, *335–336*, 216–225, doi:10.1016/j.epsl.2012.04.027.

Elliott, J. R., J. Biggs, B. Parsons, and T. J. Wright (2008), InSAR slip rate determination on the Altyn Tagh Fault, northern Tibet, in the presence of topographically correlated atmospheric delays, *Geophys. Res. Lett.*, *35*(12), n/a–n/a, doi:10.1029/2008GL033659.

Farr, T. G. et al. (2007), The Shuttle Radar Topography Mission, *Rev. Geophys.*, *45*(2), n/a–n/a, doi:10.1029/2005RG000183.

Fialko, Y., M. Simons, and D. Agnew (2001), The complete (3-D) surface displacement field in the epicentral area of the 1999 MW7.1 Hector Mine Earthquake, California, from space geodetic observations, *Geophys. Res. Lett.*, *28*(16), 3063–3066, doi:10.1029/2001GL013174.

Finnegan, N. J., M. E. Pritchard, R. B. Lohman, and P. R. Lundgren (2008), Constraints on surface deformation in the Seattle, WA, urban corridor from satellite radar interferometry time-series analysis, *Geophys. J. Int.*, *174*(1), 29–41, doi:10.1111/j.1365-246X.2008.03822.x.

Fisher, P. F., and N. J. Tate (2006), Causes and consequences of error in digital elevation models, *Prog. Phys. Geogr.*, *30*(4), 467–489, doi:10.1191/0309133306pp492ra.

Food and Agriculture Organization of the United Nations (2010), *Global forest resources assessment 2010: Main report*, Food and Agriculture Organization of the United Nations, Rome.

Food and Agriculture Organization of the United Nations (2012), *State of the world's forests, 2012*, Food and Agriculture Organization of the United Nations, Rome.

Fry, J., Dewitz, Homer C.G, Xian G, Jin S, Yang L, Barnes C.A, Herold N.D, and Wickham J.D (2011), Completion of the 2006 National Land Cover Database for the conterminous United States, *Photogramm. Eng. Remote Sens.*, *77*(9), 858–864.

Gatziolis, D., J. S. Fried, and V. S. Monleon (2010), Challenges to Estimating Tree Height via LiDAR in Closed-Canopy Forests: A Parable from Western Oregon, *For. Sci.*, *56*(2), 139–155.

Gesch, D., M. Oimoen, S. Greenlee, C. Nelson, M. Steuck, and D. Tyler (2002), The National Elevation Dataset, *Photogramm. Eng. Remote Sens.*, *68*(1), 5–11.

Goetz, S. J., A. Baccini, N. T. Laporte, T. Johns, W. Walker, J. Kellndorfer, R. A. Houghton, and M. Sun (2009), Mapping and monitoring carbon stocks with satellite observations: a comparison of methods, *Carbon Balance Manag.*, *4*(1), 2, doi:10.1186/1750-0680-4-2.

Goldstein, R. M., and C. L. Werner (1998), Radar interferogram filtering for geophysical applications, *Geophys. Res. Lett.*, *25*(21), 4035–4038, doi:10.1029/1998GL900033.

Graham, L. C. (1974), Synthetic interferometer radar for topographic mapping, *Proc. IEEE*, *62*(6), 763–768, doi:10.1109/PROC.1974.9516.

Hagberg, J. O., L. M. H. Ulander, and J. Askne (1995), Repeat-pass SAR interferometry over forested terrain, *IEEE Trans. Geosci. Remote Sens.*, *33*(2), 331–340, doi:10.1109/36.377933.

Hanssen, R. F. (2001), *Radar Interferometry: Data Interpretation and Error Analysis*, Springer, 328 pp.

Henderson, S. T., and M. E. Pritchard (2013), Decadal volcanic deformation in the Central Andes Volcanic Zone revealed by InSAR time series, *Geochem. Geophys. Geosystems*, n/a–n/a, doi:10.1002/ggge.20074.

Herrera, G., R. Tomás, F. Vicente, J. M. Lopez-Sanchez, J. J. Mallorquí, and J. Mulas (2010), Mapping ground movements in open pit mining areas using differential SAR interferometry, *Int. J. Rock Mech. Min. Sci.*, *47*(7), 1114–1125, doi:10.1016/j.ijrmms.2010.07.006.

Hetland, E. A., P. Musé, M. Simons, Y. N. Lin, P. S. Agram, and C. J. DiCaprio (2012), Multiscale InSAR Time Series (MInTS) analysis of surface deformation, *J. Geophys. Res. Solid Earth*, *117*(B2), n/a–n/a, doi:10.1029/2011JB008731.

Igarashi, T. (2001), Alos mission requirement and sensor specifications, *Adv. Space Res.*, *28*(1), 127–131, doi:10.1016/S0273-1177(01)00316-7.

Intergovernmental Panel on Climate Change, and Intergovernmental Panel on Climate Change (2007), *Climate change 2007: the physical science basis: contribution of Working Group I to the Fourth Assessment Report of the Intergovernmental Panel on Climate Change*, Cambridge University Press, Cambridge ; New York.

Izzawati, E. D. Wallington, and I. H. Woodhouse (2006), Forest Height Retrieval from Commercial X-Band SAR Products, *IEEE Trans. Geosci. Remote Sens.*, *44*(4), 863–870, doi:10.1109/TGRS.2006.870828.

Kellndorfer, J., W. Walker, L. Pierce, C. Dobson, J. A. Fites, C. Hunsaker, J. Vona, and M. Clutter (2004), Vegetation height estimation from Shuttle Radar Topography Mission and National Elevation Datasets, *Remote Sens. Environ.*, *93*(3), 339–358, doi:10.1016/j.rse.2004.07.017.

Kovats, M. (1997), A Large-Scale Aerial Photographic Technique for Measuring Tree Heights on Long-Term Forest Installations, *Photogramm. Eng. Remote Sens.*, *63*(6), 741–747.

Lefsky, M. A. (2010), A global forest canopy height map from the Moderate Resolution Imaging Spectroradiometer and the Geoscience Laser Altimeter System, *Geophys. Res. Lett.*, *37*(15), n/a–n/a, doi:10.1029/2010GL043622.

Lohman, R. B., and W. D. Barnhart (2010), Evaluation of earthquake triggering during the 2005–2008 earthquake sequence on Qeshm Island, Iran, *J. Geophys. Res. Solid Earth*, *115*(B12), n/a–n/a, doi:10.1029/2010JB007710.

Loy, W. G. (2001), *Atlas of Oregon*, 2nd ed., University of Oregon, Eugene, Or.

Lynch, J., M. Maslin, H. Balzter, and M. Sweeting (2013), Sustainability: Choose satellites to monitor deforestation, *Nature*, *496*(7445), 293–294, doi:10.1038/496293a.

Massonnet, D., M. Rossi, C. Carmona, F. Adragna, G. Peltzer, K. Feigl, and T. Rabaute (1993), The displacement field of the Landers earthquake mapped by radar interferometry, *Nature*, *364*(6433), 138–142, doi:10.1038/364138a0.

Maune, D. F. (Ed.) (2007), The National Elevation Dataset, in *Digital Elevation Model Technologies and Applications: The Dem Users Manual*, p. 655, American Society for Photogrammetry and Remote Sensing, Bethesda, MD.

Mercer, B. (2001), Combining LIDAR and IfSAR: What can you expect?, edited by D. Fritsch and R. Spiller, *Proc. Photogramm. Week 2001*, 227–237.

Pritchard, M. E. (2006), InSAR, A Tool for Measuring Earth's Surface Deformation, *Phys. Today*, *59*(7), 68–69, doi:10.1063/1.2337843.

Rosen, P., S. Hensley, and G. Peltzer (2004a), Updated Repeat Orbit Interferometry Package Released, *Eos*, *85*(5), 47.

Rosen, P. A., S. Hensley, I. R. Joughin, F. K.Li, S. N. Madsen, E. Rodriguez, and R. M. Goldstein (2000), Synthetic aperture radar interferometry, *Proc. IEEE*, *88*(3), 333–382, doi:10.1109/5.838084.

Rosen, P. A., S. Hensley, G. Peltzer, and M. Simons (2004b), Updated repeat orbit interferometry package released, *Eos Trans. Am. Geophys. Union*, *85*(5), 47–47, doi:10.1029/2004EO050004.

Rott, H. (2009), Advances in interferometric synthetic aperture radar (InSAR) in earth system science, *Prog. Phys. Geogr.*, *33*(6), 769–791, doi:10.1177/0309133309350263.

Sandberg, G., L. M. H. Ulander, J. E. S. Fransson, J. Holmgren, and T. Le Toan (2011), L- and P-band backscatter intensity for biomass retrieval in hemiboreal forest, *Remote Sens. Environ.*, *115*(11), 2874–2886, doi:10.1016/j.rse.2010.03.018.

Sarabandi, K., and Y.-C. Lin (2000), Simulation of Interferometric SAR Response for Characterizing the Scattering Phase Center Statistics of Forest Canopies, *IEEE Trans. Geosci. Remote Sens.*, *38*(1), 115–125.

Schutz, B. E., H. J. Zwally, C. A. Shuman, D. Hancock, and J. P. DiMarzio (2005), Overview of the ICESat Mission, *Geophys. Res. Lett.*, *32*(21), n/a–n/a, doi:10.1029/2005GL024009.

Sexton, J. O., T. Bax, P. Siqueira, J. J. Swenson, and S. Hensley (2009), A comparison of lidar, radar, and field measurements of canopy height in pine and hardwood forests of southeastern North America, *For. Ecol. Manag.*, *257*(3), 1136–1147, doi:10.1016/j.foreco.2008.11.022.

Solberg, S., R. Astrup, T. Gobakken, E. Næsset, and D. J. Weydahl (2010), Estimating spruce and pine biomass with interferometric X-band SAR, *Remote Sens. Environ.*, *114*(10), 2353–2360, doi:10.1016/j.rse.2010.05.011.

Treuhaft, R. N., S. N. Madsen, M. Moghaddam, and J. J. van Zyl (1996), Vegetation characteristics and underlying topography from interferometric radar, *Radio Sci.*, *31*(6), 1449–1485.

Treuhaft, R. N., B. E. Law, and G. P. Asner (2004), Forest Attributes from Radar Interferometric Structure and Its Fusion with Optical Remote Sensing, *BioScience*, *54*(6), 561–571, doi:10.1641/0006-3568(2004)054[0561:FAFRIS]2.0.CO;2.

Walker, W., J. Kellndorfer, and L. Pierce (2007), Quality assessment of SRTM C- and X-band interferometric data: Implications for the retrieval of vegetation canopy height, *Remote Sens. Environ.*, *106*, 428–448, doi:10.1016/j.rse.2006.09.007.

Wegmuller, U., and C. Werner (1997), Retrieval of Vegetation Parameters with SAR Interferometry, *IEEE Trans. Geosci. Remote Sens.*, *35*(1).

Van der Werf, G. R., D. C. Morton, R. S. DeFries, J. G. J. Olivier, P. S. Kasibhatla, R. B. Jackson, G. J. Collatz, and J. T. Randerson (2009), CO2 emissions from forest loss, *Nat. Geosci.*, *2*(11), 737–738, doi:10.1038/ngeo671.

Wickham, J. D., S. V. Stehman, L. Gass, J. Dewitz, J. A. Fry, and T. G. Wade (2013), Accuracy assessment of NLCD 2006 land cover and impervious surface, *Remote Sens. Environ.*, *130*, 294–304, doi:10.1016/j.rse.2012.12.001.

Wicks, C. W., W. Thatcher, D. Dzurisin, and J. Svarc (2006), Uplift, thermal unrest and magma intrusion at Yellowstone caldera, *Nature*, *440*(7080), 72–75, doi:10.1038/nature04507.

Williams, M. (2003), *Deforesting the earth: from prehistory to global crisis*, University of Chicago Press, Chicago, 715 pp.

Zebker, H. A., and R. M. Goldstein (1986), Topographic mapping from interferometric synthetic aperture radar observations, *J. Geophys. Res. Solid Earth*, *91*(B5), 4993–4999, doi:10.1029/JB091iB05p04993.

Zebker, H. A., and J. Villasenor (1992), Decorrelation in interferometric radar echoes, *IEEE Trans. Geosci. Remote Sens.*, *30*(5), 950–959, doi:10.1109/36.175330.